sciendo

POLISH MARITIME RESEARCH 3 (115) 2022 Vol. 29; pp. 119-127
10.2478/pomr-2022-0032

NUMERICAL STUDY OF THE EJECTION COOLING MECHANISM OF VENTILATION FOR A MARINE GAS TURBINE ENCLOSURE

Hong Shi[1]*
Qianwei Zhang[1]
Meinan Liu[1]
Kaijie Yang[2]
Jie Yuan[2]
[1] Jiangsu University of Science and Technology; China
[2] Nanjing University of Aeronautics & Astronautics; China

* Corresponding author: *shihong@nuaa.edu.cn* (Hong Shi)

ABSTRACT

A marine gas turbine enclosure must be designed to prevent overheating of the electrical and engine control components as well as diluting potential fuel leaks. In order to achieve an optimal enclosure design, a numerical study of the ventilation-ejection cooling mechanism of a gas turbine enclosure is carried out in this paper. The evaluation index of the ejection cooling performance is first proposed and the algorithm of numerical simulation is verified. On this basis, orthogonal combinations of structural parameters are carried out for the expansion angle α of the lobed nozzle and the spacing S between the outlet plane of the lobed nozzle and the inlet plane of the mixing tube. The flow and the temperature distribution inside the enclosure are analysed under different operating conditions. The results show that the influence of the lobed nozzle expansion angle α and the spacing S on the performance is not a single-valued function but the two influencing factors are mutually constrained and influenced by each other. For any spacing, the combined coefficient is optimal for the expansion angle α = 30°. When the expansion angle α = 45° and the spacing S = 100 mm, the combined coefficient and the temperature distribution inside the enclosure are optimal at the same time.

Keywords: Gas Turbine Enclosure, Ejecting Cooling, Ventilation, CFD

INTRODUCTION

A large marine gas turbine is one of the important energy conversion and transfer devices for ships. Gas turbines can use different types of fuel and emit fewer pollutants [1]. In addition, the heat from gas turbine exhaust gas can be further utilised in the thermochemical reactor and steam generator, and the water extracted from the exhaust gas can be reused for steam injection in the gas turbine cycle [2-4]. All of this makes gas turbines for marine use more competitive. Presently, the most common large marine gas turbine is the General Electric LM2500, with subsequent modifications, such as the LM2500+ and LM2500+G4. The marine gas turbines have an enclosure design with mechanical drives and other auxiliary components inside the enclosure. The enclosure not only isolates and protects the gas turbine from the external environment, but also reduces the impact of gas turbine operating noise and allows for easy maintenance and storage [5-7]. However, the closed working environment also makes it necessary to design a ventilation and cooling system for the gas turbine enclosure, to boost the power and efficiency of the gas turbine [8].

The ventilation and cooling system of a marine gas turbine enclosure prevents overheating of electrical and engine control components, as well as diluting potential fuel leaks, to eliminate stagnant areas that could lead to ignition in the cowling [9,10]. Conversely, excessive ventilation airflow may not only lead to unnecessary engine heat loss and excessive auxiliary power

requirements [11], but it may also result in excessive mixing tube outlet flow rates and, thus, additional installation costs. Therefore, optimum design of the enclosure ventilation and cooling must be based on an appropriate ventilation flow rate and temperature distribution. Traditionally, forced cooling ventilation is mostly used for cooling the enclosure, with fans providing the appropriate ventilation flow at the air inlet, which has more energy consumption in marine use. In contrast to forced cooling ventilation, ejection cooling does not require the installation of special cooling equipment and can save space in the ship design. In addition, exhaust noise can be suppressed and the intensity of infrared radiation reduced when using ejector airflow to cool the enclosure. Therefore, ejection cooling will be more widely used in marine gas turbine enclosure ventilation systems in the future [12]. However, current scholarly research is focused on forced cooling ventilation. CFD (Computational Fluid Dynamics) numerical simulations and experiments are used to obtain the distribution of airflow velocity and temperature inside the enclosure, as well as airflow organisation in the event of a gas leak [13-15]. Although there are relatively few references on the use of ejection cooling to reduce the internal temperature of gas turbine enclosures, ejecting systems have been studied relatively extensively for other applications.

Numerous studies have focused on the design of the lobed nozzle ejector and its matching with the mixing tube. Maqsood and Birk [16,17] investigated the ejecting performance of a bent ejector with a long elliptical cross-sectional area, a subsonic air-air bending ejector and an annular induced diffuser. Hu et al. [18] used PIV experiments to investigate the vortex structure and degree of turbulence in the near field of an ejector caused by a lobed nozzle. The results showed that the laminar area of the lobed nozzle is shorter and the smaller scale turbulent structures appear earlier, and are more extensive, than in the circular nozzle. Nastase and Meslem [19] found that a lobed nozzle without an expansion angle allows the improvement of mixing in the generated stream compared to a circular ejector. A lobed nozzle with an expansion angle reaches four times the entrainment of a circular ejector. Sheng [20] investigated the effect of different lobed peak spoilers on ejector performance (such as the entrainment coefficient, mixing efficiency and total pressure recovery coefficient). Varga et al. [21] found that the nozzle outlet plane influences both the critical back pressure and the entrainment coefficient. An optimum distance exists between the nozzle outlet plane and the mixing tube inlet, to allow for maximum entrainment of the secondary stream.

In summary, the lobed nozzle ejector itself and the matching of the ejector with other devices has been relatively well studied by relevant scholars. Most of the research focuses on the optimisation of the entrainment coefficient, with the objective of reducing the mainstream temperature and weakening the infrared radiation intensity, and less on the temperature distribution and pressure loss within the enclosure assembly. Although the ejection cooling is mainly based on the ejecting principle, the design objective is not only to improve the air entrainment coefficient and reduce the total pressure loss of the ejection cooling system, but also to avoid localised high temperatures in the enclosure. Therefore, the results of the above-mentioned research on ejectors cannot be simply extended to the ventilation and cooling system of the gas turbine enclosure.

Accordingly, this paper takes a marine gas turbine enclosure as the research object and proposes evaluation indexes for the cooling performance of the enclosure. The orthogonal combination method is used to obtain the ejection cooling effect under different structure parameters. Furthermore, the mechanism analysis of the flow field and temperature distribution is carried out. Finally, the optimal ventilation and cooling solution is obtained, based on the multi-objective evaluation.

GEOMETRICAL AND METHODOLOGY

GEOMETRICAL MODEL AND BOUNDARY CONDITION

In this paper, the ejection cooling system of a marine gas turbine was studied and a geometrical model established. Due to the complexity of the actual model and the limitations of computing resources, the influence of the auxiliary equipment and the piping arrangement in the enclosure were not considered when building the geometrical model. Fig.1 shows a geometrical model reflecting the main features of the gas turbine casing.

The *Realizable k-ε* turbulence model was used in the CFD numerical simulation. Meanwhile, the equations of mass, momentum, turbulence kinetic energy and dissipation rate were solved using the SIMPLE (Semi-Implicit Method for Pressure Linked Equation) algorithm. The airflow properties were taken to be those for an ideal gas and the temperature was defined in sections, according to the state of the gas turbine operation. The surface of the high-temperature components of the gas turbine was coated with thermal protection material and the gas turbine casing set up as a slip-free wall, with an emissivity of 0.9 [22].

Furthermore, the exhaust plenum outlet was set up as a mass flow inlet with a mass flow rate of 27.8 kg/s and temperature of 782 K. The cooling inlet was set up as a pressure inlet with a temperature of 300 K and a pressure of 0 Pa. The mixing tube outlet was set up as a pressure outlet with a temperature of 300 K and a pressure of 1000 Pa.

Fig.2 shows the structure of the lobed nozzle ejector and the ejection cooling system.

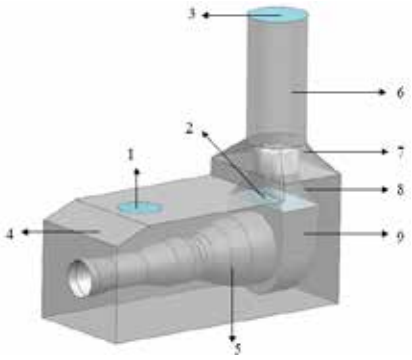

(a) Enclosure geometrical model:
1 - Cooling inlet (Secondary stream inlet);
2 - Exhaust plenum outlet (Mainstream inlet);
3 - Mixing tube outlet (Mixed streams outlet);
4 - Gas turbine enclosure;
5 - Gas turbine casing;
6 - Mixing tube;
7 - Transition section (Between the mixing tube and the enclosure);
8 - Lobed nozzle ejector;
9 - Exhaust plenum.

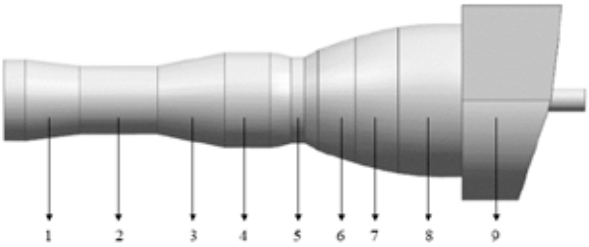

(b) Gas turbine casing geometrical model:
1 - Inlet section 350 K;
2 - Low pressure air compressor 400 K;
3 - High pressure air compressor 550 K;
4 - Combustion 600 K;
5 - Aft combustion chamber 500 K;
6 - Transition section700 K;
7 - Power turbine 400 K;
8 - Aft power turbine 400 K;
9 - Exhaust plenum 390 K.

Fig. 1. Geometrical model

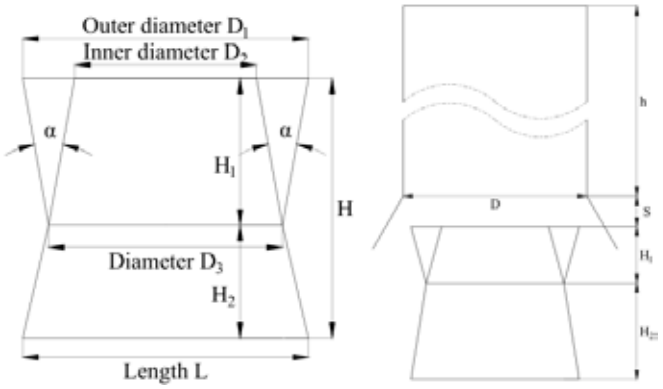

(a) Lobed nozzle ejector *(b) Ejection cooling system*

Fig. 2. Schematic of the structure

The lobed nozzle expansion angle α and the spacing S between the outlet of the lobed nozzle and the inlet of the mixing tube were set up as an orthogonal combination of structural parameters. Unlike traditional lobed nozzle ejectors, the lobed nozzle ejector studied in this paper consisted of a lobed nozzle section (H_1) and a square-to-circle section (H_2), as shown in Fig.2(a). As the exhaust plenum outlet plane is square, the lobed nozzle needed to be designed with a square-to-circle section, to connect the square plane of the exhaust plenum outlet to the circle plane at the bottom of the lobed nozzle.

It should be noted that, because the lobed nozzle ejector and the gas turbine enclosure were matched to each other, the total height (H) of the lobed nozzle ejector remained constant during the structural analysis of the lobed nozzle ejector. Therefore, when designing different expansion angles α by varying the lobed nozzle height (H_1), the change in lobed nozzle height (H_1) caused a change in the height of the square-to-circle height (H_2). There is a matching relationship between the two sections.

As shown in Fig.2(b), the spacing between the outlet of the lobed nozzle ejector and the inlet of the mixing tube is S. Specifically, S < 0 mm means that the ejector outlet is inside the mixing tube. S = 0 mm means that the ejector outlet is in the same plane as the mixing tube inlet. S > 0 mm means that there is a distance between the ejector outlet and the mixing tube inlet.

The fixed parameters of the ejector and mixing tube structure were designed as shown in Table.1.

Tab. 1. Fixed parameters

Design content			Parameter settings
Ejector	Ejector	Total height	1000 mm
	Lobed nozzle section (H_1)	Outlet area	591323 mm^2
		Width of the lobe	100 mm
		Outer diameter (D_1)/ Inner diameter (D_2)	D_1 = 1100 mm, D_2 = 700 mm
		Diameter of the bottom circular surface (D_3)	900 mm
		Number of the lobe	10 (Evenly distributed by circumference)
	Square-to-circle section (H_2)	Exhaust plenum outlet plane	1100 mm × 2000 mm
Mixing tube	Diameter (D)		1200 mm

Based on the fixed parameters in Table 1, orthogonal combinations were performed for four different lobed nozzle expansion angles α and six different spacings S, for a total of 24 combinations. Specifically, the expansion angle α of Case 1 - Case 6 was 20° and the spacings were: -100 mm, 0 mm, 100 mm, 200 mm, 400 mm, 500 mm, respectively. The expansion angle α for Case 7 - Case 12 was 30° and

the spacings were as above. The expansion angle α for Case 13 - Case 18 was 45° and the spacings were as before. The expansion angle α for Case 19 - Case 24 was 60° and the spacings were as above.

EVALUATION INDICATORS

System Performance Indicators

Due to space limitations in the ship, it is difficult to achieve the optimum mixing tube lengths for the ejector design. At the same time, considering the mixing loss between the mainstream and secondary streams, the maximum entrainment coefficient should not be pursued while meeting the cooling requirements of the gas turbine enclosure [23]. The entrainment coefficient and pressure are closely related to the temperature field. Therefore, in the actual program selection process, the flow field calculation can be performed first, to obtain a series of cases that meet the requirements, and then temperature field checks can be carried out. This method makes the calculation relatively efficient.

In this paper, the entrainment coefficient was combined with the pressure loss coefficient in the flow field calculation, to obtain the combined coefficient, and it was used as an evaluation indicator for the flow characteristics of the ejection cooling system. The implication of the combined coefficient is that a better system performance should provide a higher entrainment coefficient at a lower pressure loss. The equation is as follows:

$$Combined\ coefficient = \frac{Entrainment\ coefficient}{Pressure\ loss\ coefficient} \quad (1)$$

– Entrainment coefficient

The entrainment coefficient is a dimensionless coefficient that indicates the entrainment capacity of the ejection cooling system, and is defined as follows:

$$n = \frac{G_2}{G_1} \quad (2)$$

where G_1 is the mass flow rate of the mainstream, and G_2 is the mass flow rate of the secondary stream.

– Pressure loss coefficient

The pressure loss coefficient is a dimensionless coefficient which indicates the flow loss in the ejection cooling system and is expressed as follows:

$$\prod = \frac{P_1 - P_2}{q} \quad (3)$$

where P_1 is the total pressure at the outlet of the exhaust plenum, P_2 is the total pressure at the outlet of the mixing tube, and q is the dynamic pressure at the outlet of the exhaust plenum.

Temperature Indicators

The air temperature in a typical plane within the enclosure needs to be less than 82°C (355 K) during operations [24]. It should be noted that, due to the high temperature of the gas turbine casing, it is difficult to significantly reduce the temperature in the section near the gas turbine casing by ejection cooling alone. Therefore, the temperature in the section near the gas turbine casing does not have to be considered within the required temperature indicators.

ALGORITHM VALIDATION

In order to ensure the reliability of the numerical simulations in this paper, a geometric model was built based on the parameters in the literature [25]. For the numerical simulation, the experimental system was simplified and only the lobed nozzle section was retained, as shown in Fig.3. Specifically, the outer diameter of the outlet plane of the lobed nozzle is 108.0 mm, the inner diameter is 54.0 mm, and the diameter of the inlet plane is 70 mm. The height of the lobed nozzle is 73 mm, the width of each lobe is 7.2 mm, and the number of lobes is 12. The boundary conditions of the numerical simulation were based on the experiments in the literature. Specifically, the mainstream inlet was set as the velocity inlet with a velocity of 21 m/s and a temperature of 620 K. The secondary stream inlet and the mixing outlet were simultaneously set as pressure boundaries, with an ambient pressure and a temperature of 300 K. The results of the experiments and simulations are shown in Fig.4.

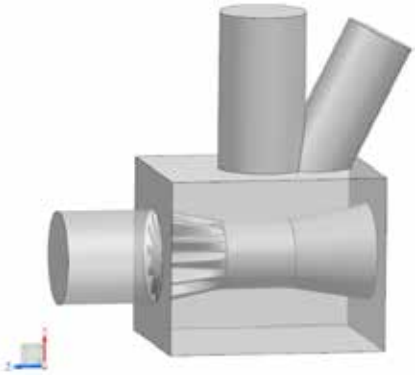

Fig. 3. Geometric model

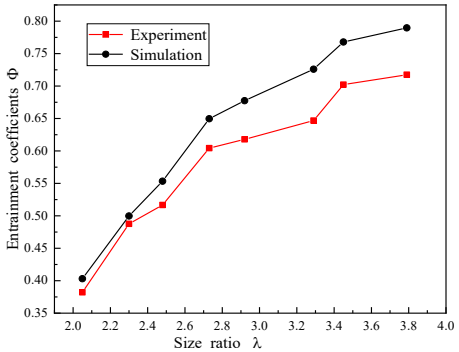

Fig. 4. Experiments and simulations

As shown in Fig.4, the simulation results are slightly higher than the experimental results. The main reason for this is that, in the experiments, the mainstream inlet of the lobed nozzle ejector is equipped with piping in front of it, which may lead to a non-uniform distribution of the mainstream velocity. In the simulations, however, the mainstream velocity is designed to be uniformly distributed. Therefore, there is a difference between the simulated and experimental mainstream inlets. Because the difference in the results of the entrainment coefficient in the experiments and simulations is less than 10%, for different size ratios, and the variation trend is relatively consistent, the numerical simulation of the ejector (in this paper) has some reliability and can be used for subsequent studies.

MESH INDEPENDENCE

An unstructured polyhedral mesh was created for the geometric model, with mesh refinement in more complex areas, such as the inlet and outlet of the model and the lobed nozzle ejector. At the same time, a boundary layer was created on the mixing tube and the gas turbine casing. In order to ensure that the results were independent of the number of meshes, when analysing the performance of the system, the geometric model of Case 3 (α = 20°, S = 100 mm) was chosen to create meshes of five different diameters. The effect of different diameters of meshes on the performance of the system was analysed using the total pressure of the mainstream inlet and the average temperature of the central plane as indicators. The results are shown in Table 2.

Tab. 2. Mesh independence validation

Number of meshes	2.05 million	3.37 million	4.70 million	5.88 million	6.75 million
Total pressure of the mainstream inlet (Pa)	3549.7	3684.4	3744.3	3748.4	3746.9
Average temperature of the central plane (K)	313.4	315.1	315.6	315.7	315.6

As shown in Table 2, when the number of meshes reaches 4.70 million, the total pressure at the mainstream inlet and the average temperature at the central plane hardly change as the mesh number increases. Considering the speed of the simulation and the accuracy of the results, a mesh with the number of 4.70 million was chosen for the subsequent simulations in this paper.

SIMULATION AND RESULTS

COMBINED COEFFICIENT

Fig.5 shows the variation pattern of the combined coefficient with the lobed nozzle expansion angle α and spacing S.

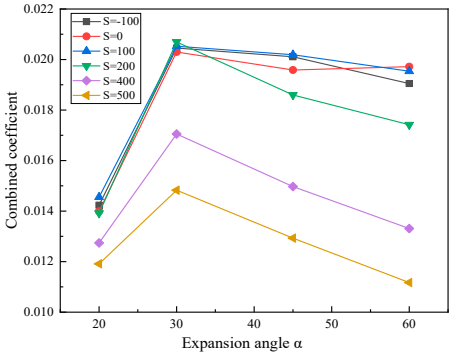

Fig. 5. Combined coefficient variation pattern

As shown in Fig.5, with the increase of the expansion angle α, the combined coefficient first increases and then decreases. When the expansion angle α = 20°, the ejector structure results in a high total pressure loss and, therefore, the combined coefficient remains low. For any spacing, the combined coefficient is optimal for the expansion angle α = 30°. Of the 24 cases, the four cases with the best combined coefficients are Case 7 (α = 30°, S = -100 mm), Case 9 (α = 30°, S = 100 mm), Case 10 (α = 30°, S = 200 mm), and Case 15 (α = 45°, S = 100 mm), with Case 10 having the best combined coefficient of them all. The following is a specific analysis, in terms of both the entrainment coefficient and the pressure loss coefficient.

Entrainment Coefficient

Fig.6 shows the variation pattern of the entrainment coefficient with the expansion angle α and spacing S.

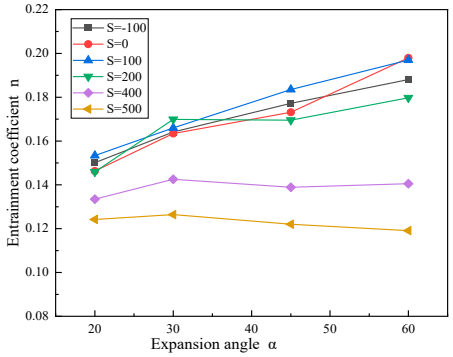

Fig. 6. Entrainment coefficient variation pattern

From Fig.6, it can be seen that there are two trends in the entrainment coefficient, with different expansion angles α and spacing S.

(1) When the spacing S ≤ 100 mm, the entrainment coefficient increases with increasing expansion angle α.

In order to further study the mechanism of the effect of the expansion angle α on the entrainment coefficient, the velocity distribution and stream-wise vortices are specifically analysed for a spacing S = 0 mm. Fig.7 shows the velocity distribution of the ejector.

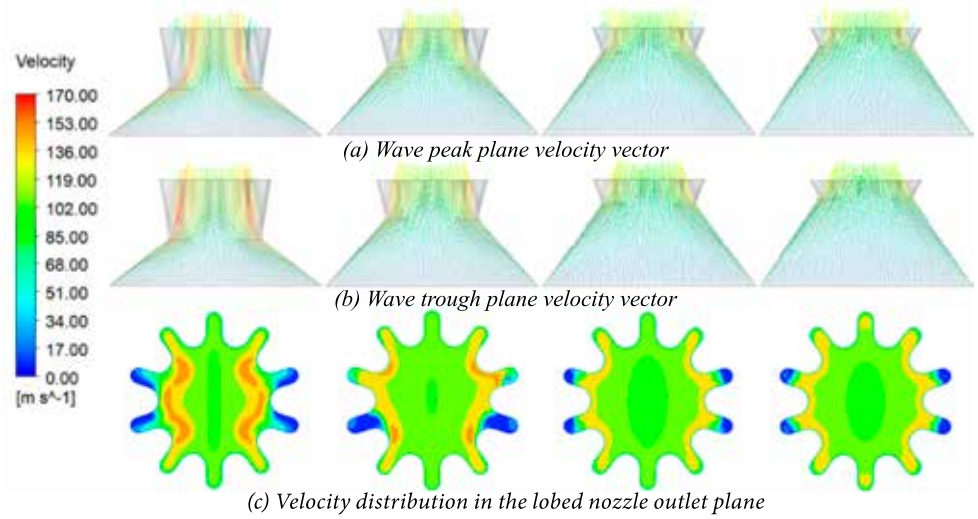

(a) Wave peak plane velocity vector

(b) Wave trough plane velocity vector

(c) Velocity distribution in the lobed nozzle outlet plane

Fig. 7. Velocity of the lobed nozzle ejector plane (From left to right : 20°, 30°, 45°, 60°)

As shown in Fig.7, due to the influence of the square-to-circle section (H_2) of the ejector, the mainstream velocity distribution within the ejector is not uniform and localised high velocity areas can exist near the walls. When the expansion angle α = 20°, the height of the square-to-circle section (H_2) is the smallest, the deformation in the length direction is the most intense, and the backflow area at the lobe boundary is larger. As the expansion angle α increases, the height of the square-to-circle section (H_2) gradually increases, and the deformation between the length direction of the exhaust plenum outlet and the circle plane at the bottom of the lobed nozzle is gradually eased. Meanwhile, the velocity of the mainstream gradually decreases along the walls and the velocity distribution inside the ejector tends to be uniform. In addition, as the height of the lobed nozzle section (H_1) gradually decreases, the backflow area within the lobed nozzle also gradually decreases and the utilisation of the mainstream gradually increases. Thus, as the expansion angle α increases, the entrainment coefficient gradually rises.

(2) When the spacing S ≥ 200 mm, the entrainment coefficient fluctuates with increasing expansion angle α.

Taking the expansion angle α = 45° as an example, Fig.8 shows the velocity vector in the inlet area of the mixing tube for spacings of 200 mm, 400 mm, and 500 mm.

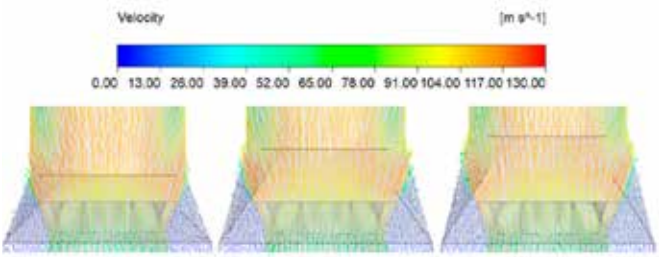

Fig. 8. Velocity vector in the mixing tube inlet area (From left to right : 200 mm, 400 mm, 500 mm)

As shown in Fig.8, when the spacing S = 200 mm, the mainstream begins to diffuse fully as it reaches the mixing tube inlet, with a small proportion of the mainstream impacting the wall of the transition section in front of the mixing tube inlet. These block the passage of the secondary stream into the mixing tube and the wall of the transition section has an inclined angle, which causes the secondary stream to randomly return to the interior of the enclosure, thus reducing the entrainment coefficient. When the expansion angle α changes, the impact point of the mainstream and transition section changes, resulting in fluctuations in the entrainment coefficient. However, when the spacing S = 200 mm, there is relatively little backflow and so the entrainment coefficient remains at a high level.

As the spacing S increases further, the passage from the ejector outlet plane to the inlet plane of the mixing tube gradually widens and the mainstream is fully diffused before it reaches the inlet of the mixing tube. The impact of the mainstream on the transition section wall reduces the utilisation of the mainstream and blocks the passage of the secondary stream, making the backflow of the secondary stream more serious. Therefore, the entrainment coefficient is generally low when the spacing S is large. The degree of backflow and passage blockage of the secondary stream depends on the matching relationship between the expansion angle α and the mixing tube. As the structure of the ejector and the transition section in front of the mixing tube do not vary in a univariate manner, the entrainment coefficient fluctuates with the expansion angle α, but does not vary significantly.

Pressure Loss Coefficient

Fig.9 shows the variation pattern of the pressure loss coefficient with the lobed nozzle expansion angle α and the spacing S.

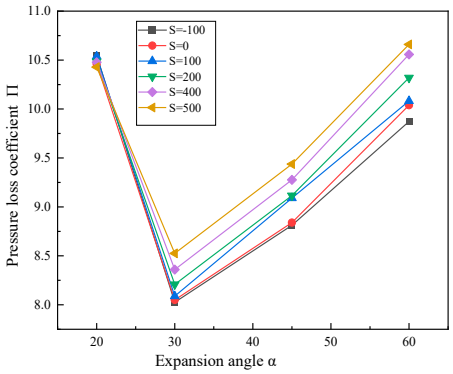

Fig. 9. Pressure loss coefficient variation pattern

As can be seen from Fig. 9, the pressure loss coefficient follows the same trend at different spacings. This means that, as the expansion angle α increases, the pressure loss coefficient at any spacing S shows a tendency to decrease and then increase. Specifically, the pressure loss coefficient decreases rapidly as the expansion angle α increases from 20° to 30°. As the expansion angle α increases further, the pressure loss coefficient gradually increases.

In order to further study the mechanism of the effect of the expansion angle α on the pressure loss coefficient, a pressure loss table is presented, for specific analysis. Using the spacing S = 0 mm as an example, Table 3 shows the total pressure loss of the ejection cooling system.

Tab. 3. Total pressure loss in the ejection cooling system

Spacing (S) / mm	Expansion angle (α)	Total pressure loss inside the ejector / Pa			Total pressure loss in the ejection cooling system / Pa		
		Lobed nozzle section (H_1)	Square-to-circle section (H_2)	Total pressure loss	Exhaust plenum outlet plane	Mixing tube outlet plane	Total pressure loss
0	20°	553.49	400.08	953.57	3719.74	1910.49	1809.25
	30°	303.87	164.73	468.60	3418.68	1923.11	1495.57
	45°	295.37	124.29	419.66	3454.36	1932.77	1521.59
	60°	327.39	100.80	428.19	3693.55	1971.37	1722.18

As can be seen from Table 3, two important mechanisms contribute to the total pressure loss in the ejector. These are: non-uniformity of the mainstream velocity, due to the sharp geometrical deformation of the square-to-circle part (H_2) of the ejector, and intense mixing, due to the enhanced entrainment capacity. Specifically, as the expansion angle α increases, the total pressure loss in the square-to-circle section (H_2) gradually decreases. At an expansion angle α = 20°, the total pressure loss in the square-to-circle section (H_2) is the highest, at approximately 400.08 Pa. The main reason for this is that the square-to-circle section (H_2) achieves a sharp square to circle transition at a relatively short height. The large change in geometry leads to a non-uniform mainstream velocity which, in turn, leads to large pressure loss. As the square-to-circle section (H_2) gradually increases, the deformation is gradually eased and the local pressure loss is reduced. However, when the expansion angle α = 60°, the entrainment capacity increases significantly and the energy consumed by the entrained secondary stream also increases significantly, resulting in a higher total pressure loss in the lobed nozzle section (H_1).

TEMPERATURE DISTRIBUTION

For the study of the gas turbine ejection cooling system, in addition to obtaining a better combined coefficient, it is equally important to reduce the high temperature areas inside the enclosure. Therefore, this section provides a specific analysis of the temperature distribution in typical planes inside the enclosure for the four cases with the better combined coefficients. Fig.10 shows the temperature distribution in typical planes inside the enclosure for each of the four cases.

As shown in Fig.10, the airflow enters the enclosure from the cooling inlet and flows to the gas turbine casing surface and, subsequently, along the gas turbine surface below. Therefore, the temperature of the airflow directly below the cooling inlet is lower. As the space inside the enclosure increases, the airflow velocity gradually decreases and, combined with the radiation from the high temperature of the gas turbine casing surface, the airflow is further heated inside the enclosure.

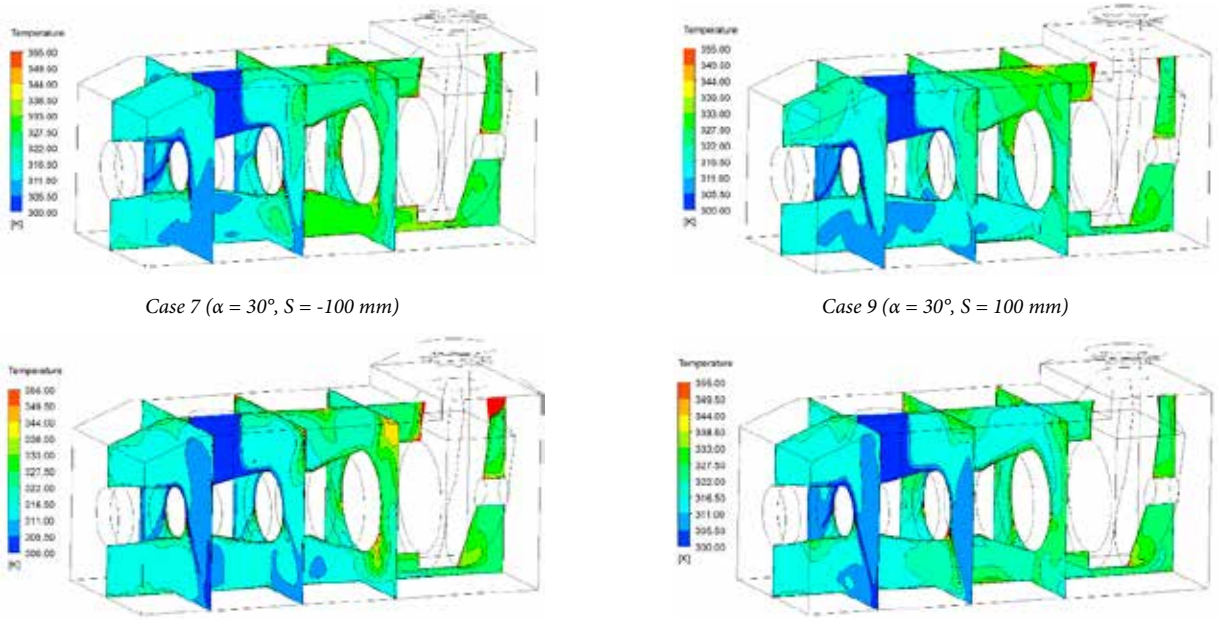

Case 7 (α = 30°, S = -100 mm)

Case 9 (α = 30°, S = 100 mm)

Case 10 (α = 30°, S = 200 mm)

Case 15 (α = 45°, S = 100 mm)

Fig. 10. Temperature distribution in typical planes

However, in Case 7, Case 9 and Case 10, there are localised areas with high temperatures on the top wall of the enclosure. This is because, as the spacing S increases, the backflow near the ejector inside the enclosure gradually becomes more serious. At the same time, more high temperature areas are generated inside the enclosure. In Case 15, the relatively high entrainment coefficient results in relatively high airflow velocities inside the enclosure and a relatively low temperature in the enclosure, with no high temperature areas inside the enclosure. On balance, Case 15 is the preferred option.

CONCLUSION

In this paper, a numerical study was carried out on the ventilation and cooling system of a gas turbine enclosure. The analysis focused on the effects of different expansion angles α and the spacing S between the lobed nozzle outlet plane and the mixing tube inlet plane on the ventilation and cooling performance. The combined coefficients of the ejection cooling system and the temperature distribution inside the enclosure under different design parameters were obtained and analysed specifically. The specific findings of this paper are as follows.

(1) The influence of the expansion angle α and the spacing S on performance is not a single-valued function, but the two influencing factors are mutually constrained and influenced by each other. The main reason for this is that the mixing tube in the enclosure and the square-to-circle section (H_2) interfere with the performance of the ejector, which differs significantly from a conventional ejector.

(2) The sharp reduction in height of the square-to-circle section (H_2) leads to the existence of a low velocity backflow area in the lobed nozzle, causing a blocking effect on the mainstream. However, as the expansion angle α increases, the backflow area within the lobed nozzle gradually decreases, and the utilisation of the mainstream gradually increases, more secondary streams can be entrained.

(3) For any spacing, the optimal combined coefficient is obtained for an expansion angle α = 30°. However, in the case of the better solution, there may still be localised high temperature areas inside the enclosure. So, four cases with the best combined coefficients are selected before the local temperature distribution analysis, namely Case 7, Case 9, Case 10 and Case 15. Through comparison and analysis, Case 15 has a better combined coefficient and there are no high temperature areas inside the enclosure, therefore Case 15 is the preferred option.

REFERENCES

1. N.R. Ammar and A. Farag, "CFD Modeling of Syngas Combustion and Emissions for Marine Gas Turbine Applications" Polish Maritime Research, vol.23, no.3, pp.39-49, 2016. doi: 10.1515/pomr-2016-0030.
2. O. Cherednichenko, S. Serbin, and M. Dzida, "Application of Thermo-chemical Technologies for Conversion of Associated Gas in Diesel-Gas Turbine Installations for Oil and Gas Floating Units," Polish Maritime Research, vol. 26, no. 3, 2019. doi: 10.2478/pomr-2019-0059.
3. S. Serbin, K. Burunsuz, M. Dzida, J. Kowalski, and D. Chen, "Investigation of Ecological Parameters of a Gas Turbine Combustion Chamber with Steam Injection for the Floating Production, Storage, and Offloading Vessel," International Journal of Energy and Environmental Engineering, 2021. doi: 10.1007/s40095-021-00433-w.
4. S. Serbin, N. Washchilenko, M. Dzida, and J. Kowalski, "Parametric Analysis of the Efficiency of the Combined Gas-Steam Turbine Unit of a Hybrid Cycle for the FPSO Vessel," Polish Maritime Research, vol. 28, no. 4, 2022. doi: 10.2478/pomr-2021-0054.
5. O. Kyrylash, V. Kostiuk, A. Smirnov, D. Tkachenko, and I.Loboda, "Mathematical Simulation of the Gas Turbine Packages Thermal State." Proceedings of the ASME Turbo Expo 2018: Turbomachinery Technical Conference and Exposition. vol.5C, Oslo, Norway. June 11-15, 2018. doi: 10.1115/GT2018-77194.
6. J. Kowalski, F. Di Mare, S. Theis, A. Wiedermann, M. Lange, and R. Mailach, "Investigation of the Ventilation Flow in a Gas Turbine Package Enclosure." European Conference on Turbomachinery Fluid Dynamics and Thermodynamics, 2019. doi: 10.29008/ETC2019-438.
7. A. Corsini, G. Delibra, M. Giovannelli, G. Lucherini, S. Minotti, S. Rossin, and L. Tieghi, «Prediction of Ventilation Effectiveness for LM9000 Package with Machine Learning.» Proceedings of the ASME Turbo Expo 2020: Turbomachinery Technical Conference and Exposition. vol.9. Virtual, online. September 21-25, 2020. doi: 10.1115/GT2020-14916.
8. Z. Domachowski, and M. Dzida, "Applicability of Inlet Air Fogging to Marine Gas Turbine" Polish Maritime Research, vol.26, no.1, pp.15-19, 2019. doi: 10.2478/pomr-2019-0002.
9. International Standard ISO 21789:2009 Gas Turbine Applications – Safety, International Organisation for Standardization, 2009.
10. G. Lucherini, V. Michelassi, and S. Minotti, "The Impact of Model Assumptions on the CFD Assisted Design of Gas Turbine Packages." Proceedings of the ASME Turbo Expo 2019: Turbomachinery Technical Conference and Exposition. vol.9. USA. June 17-21, 2019. doi: 10.1115/GT2019-90871.
11. R. Yerram, R. Watkins, and B. Ponnuraj, "Aeroderivative Gas Turbine Enclosure Ventilation System." Proceedings of the ASME Turbo Expo 2021: Turbomachinery Technical Conference and Exposition. vol.2C. Virtual, online. June 7-11, 2021. doi: /10.1115/GT2021-59136.

12. D.M. Li, L. Wang, X.Y. Wen, and S.D. Cao, "Numerical Simulation and Experimental Study of Marine Combustion Engine Exhaust Ejector." Thermal Power Engineering, vol.17, no.3, pp.226-230, 2002. doi: 10.3969/j.issn.1001-2060.2002.03.002.

13. B. Ponnuraj, B. Sultanian, A. Novori, and P. Pecchi, "3D CFD Analysis of an Industrial Gas Turbine Compartment Ventilation System." Proceedings of the ASME 2003 International Mechanical Engineering Congress and Exposition. Heat Transfer, vol.2. Washington, DC, USA. November 15–21, 2003. pp. 67-76. ASME. doi: 10.1115/IMECE2003-41672.

14. E. Graf, T. Luce, and F. Willett, "Design Improvements Suggested by Computational Flow and Thermal Analyses for the Cooling of Marine Gas Turbine Enclosures." Proceedings of the ASME Turbo Expo 2005: Power for Land, Sea, and Air. vol.5. Reno, Nevada, USA. June 6-9, 2005. pp. 587-593. doi: 10.1115/GT2005-68574.

15. G. Lucherini, S. Minotti, G. Ragni, and F. Bologna, "Experimental and Numerical Investigation on Gas Turbine Package Scale Model." Proceedings of the ASME Turbo Expo 2018: Turbomachinery Technical Conference and Exposition. vol.9. Oslo, Norway. June 11-15, 2018. doi: 10.1115/GT2018-75694.

16. A. Maqsood, and A.M. Birk, "Effect of a Bend on the Performance of an Oblong Ejector." Proceedings of the ASME Turbo Expo 2007: Power for Land, Sea, and Air. vol.6. Montreal, Canada. May 14-17, 2007. pp.37-45. doi: 10.1115/GT2007-27851.

17. A. Maqsood, and A.M. Birk, "Effect of Entraining Diffuser on the Performance of Bent Exhaust Ejectors." Proceedings of the ASME Turbo Expo 2010: Power for Land, Sea, and Air. vol.7. Glasgow, UK. June 14-18, 2010. pp.2793-2802. doi: 10.1115/GT2010-23499.

18. H. Hu, T. Saga, T. Kobayashi, and N. Taniguchi, "Research on the Vortical and Turbulent Structures in the Lobed Jet Flow Using Laser Induced Fluorescence and Particle Image Velocimetry Techniques." Measurement Science & Technology, vol.11, no.6, p.698, 2000. doi: 10.1088/0957-0233/11/6/313.

19. I. Nastase and A. Meslem, "Passive Control of Jet Flows Using Lobed Nozzle Geometries." Mecanique Et Industries, vol.8, no.2, pp.101-109, 2007. doi: 10.1051/meca:2007027.

20. Z.Q. Sheng, "Jet Mixing of Lobed Nozzles with Spoilers Located at Lobe Peaks." Applied Thermal Engineering, vol.119, pp.165-175, 2017. doi: 10.1016/j.applthermaleng.2017.03.048.

21. S. Varga, A.C. Oliveira, and B. Diaconu, "Influence of Geometrical Factors on Steam Ejector Performance – A Numerical Assessment." International Journal of Refrigeration, vol.32, no.7, pp.1694-1701, 2009. doi: 10.1016/j.ijrefrig.2009.05.009.

22. Z.B. Zhang, X.Y. Zhang, B.B. Li, and P. Sun, "Optimal Design of Cooling Structure of an Industrial Type Gas Turbine Enclosure Mount." Thermal Science and Technology, vol.5, no.7, 2016. doi: 10.13738/j.issn.1671-8097.2016.05.013.

23. Y.L. Han, "Numerical Simulation and Experimental Study of Marine Gas Turbine Exhaust Ejector." Diss. Harbin Engineering University, 2005, doi: 10.7666/d.y780039.

24. H. Bagheri and D. Vahidi, "Ventilation of Gas Turbine Package Enclosures: Design Evaluation Procedure." 25th International Conference on Offshore Mechanics and Arctic Engineering, 2006.

25. Y.H. Liu, "Experimental Study and Numerical Simulation of Wave Flap Induced Mixer in Hot and Cold State." Diss. Nanjing University of Aeronautics and Astronautics, 2000. doi: 10.7666/d.y400568.

CONTACT WITH THE AUTHORS

Hong Shi

Jiangsu University of Science and Technology;
College of Energy & Power Engineering; Zhenjiang,
China

Qianwei Zhang

Jiangsu University of Science and Technology;
College of Energy & Power Engineering; Zhenjiang,
China

Meinan Liu

Jiangsu University of Science and Technology;
College of Energy & Power Engineering; Zhenjiang,
China

Kaijie Yang

Nanjing University of Aeronautics & Astronautics;
Key Laboratory of Aircraft environment control
and life support, MIIT; Nanjing,
China

Jie Yuan

Nanjing University of Aeronautics & Astronautics;
Key Laboratory of Aircraft environment control
and life support, MIIT; Nanjing,
China

sciendo

POLISH MARITIME RESEARCH 3 (115) 2022 Vol. 29; pp. 128-140
10.2478/pomr-2022-0033

MONITORING THE PERFORMANCE OF A SHIP'S MAIN ENGINE BASED ON BIG DATA TECHNOLOGY

Meng Liang*
Shanghai Dianji University, Business School, Shanghai, China
Mingzhi Chen
Shanghai Maritime University, Merchant Marine College and Shanghai Engineering Research Center of Ship Intelligent Maintenance and Energy Efficiency, China

* *Corresponding author: liangmeng02@163.com (Meng Liang)*

ABSTRACT

Under the recent background of 'Green Shipping' and rising fuel prices, it is very important to reduce the fuel consumption rate of ships, which is directly affected by the performance of the main engine. A reasonable maintenance schedule can optimise the performance of the main engine. However, a traditional maintenance schedule is based on the navigation distance and time, ignoring many other factors, such as a harsh working environments and frequently changing operating conditions, which will lead to faster performance degradation. In this study, a real-time evaluation method combing big data of ship energy efficiency with physics-based analysis is proposed to judge the degradation of main engine performance and assist in determining the maintenance schedule. Firstly, based on the developed ship energy efficiency big data platform, the distribution statistics and comparison of different operating states are carried out. Gaussian mixture model (GMM) and Density-Based Spatial Clustering of Applications with Noise (DBSCAN) are used to cluster the data and the high-density data areas are obtained as the analysis points. Then, the data of the analysis points are polynomial fitted, by the least square method, to obtain the propulsion characteristics curves, load characteristic curves, and speed characteristic curves, which can be used to observe the performance degradation of the main engine. The results show that this method can effectively monitor the degradation degree of the main engine performance, and is of great significance to fuel efficiency improvements and greenhouse gas (GHG) emissions reduction.

Keywords: Big data of ship energy efficiency, Main engine, Performance evaluation, Cluster analysis, Mechanism analysis

INTRODUCTION

Ocean transport is vital for global trade and more than 90% of international cargo is transported by the international shipping industry [1]. Despite its significance, however, the great amount of fuel consumption and air pollutants caused by the shipping industry are more and more severe. The main air pollutants caused by shipping include nitrogen oxides (NOx), sulphur oxides (SOx), harmful particulate matter (PM), and greenhouse gas (mainly CO_2). According to the publications of the International Maritime Organisation (IMO), international shipping accounts for 14-31%, 4-10%, and 2-3% of the total worldwide global emissions of NOx, SOx, and CO_2, respectively [2].

The IMO has issued a series of regulations to restrict the emission of air pollutants from shipping because they are aware of the seriousness of the problem. The shipping industry has also taken a series of measures to reduce emissions. The scrubber system is an alternative measure to reduce SOx emissions, although it requires a large amount of cabin space, is complex and expensive to operate [3]. An SCR (Selective Catalytic Reduction) reactor can be used for reducing NOx emissions. However, carbon capture and other CO_2 emission reduction equipment are far less mature than scrubber systems and SCR reactors and not commonly used. Alternative fuels, such as biofuels and hydrogen, are promising developments but there are still some concerns about their storage, technology maturity, and safety mitigation measures

in the current situation. Therefore, reducing fuel consumption remains the top priority in controlling greenhouse gas (GHG) emissions for ships in service.

Meanwhile, IMO has put forward more and more regulations concerning CO_2 emissions from ships, prompting international shipping companies to put in place technological and operational measures. In 2011, the Energy Efficiency Design Index (EEDI) [4] was proposed to urge shipping companies to meet basic energy efficiency requirements when building new ships and the Ship Energy Efficiency Management Plan (SEEMP) [5] was put forward in the same year (specific ship operational measures to reduce emissions). In late 2020, IMO approved the MARPOL Annex VI amendment, which requires all existing ships to satisfy both the Efficiency Existing Ship Index (EEXI) and Carbon Intensity Indicator (CII) requirements, as well [6]. This represents the IMO's follow-up action plan for reducing GHG emissions from international shipping vessels up to 2050. Since exhaust gas emission is difficult to measure directly, and is generally proportional to fuel consumption, the regulation for European ships' Monitoring, Reporting, and Verification (MRV) provides indirect monitoring through the ship's fuel consumption [7].

For a ship, the consumption of fuel mainly depends on two factors: the operating efficiency of the main propulsion system and the motion resistance [8]. Król summarised the current technical status of propeller system design and operation with the installation of energy-saving devices [9]. Puzdrowska paid attention to the problem of low controllability of marine medium and high-speed engines during operation, and proposed measures for quickly controlling the temperature of exhaust gas [10]. Król presented a simplified lifting surface method in propeller design [11]. Rudzki et al. proposed a decision-making system to select commands for the ship's propulsion system with a controllable pitch propeller [12]. Varbanets et al. provided a method to accurately measure the top dead centre (TDC) [13]. All of the above studies have laid an important foundation for performance improvements in ship propulsion systems.

It is widely known that the main engine is the main propulsion system overcoming the total resistance from the cargo dead weight, draft, trim, sea weather, etc. [14], to propel the ship forward. The main engine produces the original thrust through fuel consumption and pushes the propeller through a series of transmission devices to overcome the resistance [15]. As the original power of a ship, the performance of the main engine directly affects the fuel consumption rate. Customising a scientific maintenance schedule for the main engine can guarantee its good performance. However, a traditional maintenance schedule usually relies on the total navigation distance or time, without the consideration of many other environmental factors such as humidity, oscillatory working conditions, the switching of operating conditions, or weather changes on the voyage, etc.

This study aims to evaluate the performance degradation of the main engine in real-time through big data of navigation processes, such as ship fuel consumption, marine main engine status, ship status, and cargo loading status. The maintenance schedule, based on the results analysed, considers more factors and is more in line with the actual circumstances. To analyse the behaviour of marine diesel engines in different unsteady states (e.g. determining fuel consumption rate), Ghaemi proposed a goal-based mathematical model and provided a method for determining the model parameters through the available data provided by the engine manufacturer [16]. However, data are still limited.

As one of the most traditional industries, the shipping industry still relies more on intuition than on data [17]. A small amount of original voyage data comes from the ship's noon report, but this data has many flaws, such as manual recording errors, long time intervals, and small amounts of data acquisition, which is not conducive to subsequent analysis [18]. Fortunately, the Internet of Things (IoT), data transmission technology, and big-data technology under the background of 'Industry 4.0', provide a promising approach for voyage data collection and transmission [19]. Fan et al. designed a multi-source information system to collect data related to a ship's energy consumption and navigation environment [20]. Deng et al. analysed and predicted the energy efficiency of ships, based on 6G communication technology, which can access the data in real-time [21]. Both of them focused on inland river ships. Tacjana et al. monitored the heat exchanger in a steam power plant through machine learning algorithms, which shows that machine learning is a measure worthy of research and application [22]. Witkowska et al. presented a multi-dimensional nonlinear dynamic positioning (DP) controller, which adopts the adaptive vector back-stepping method and Radial Basis Function (RBF) artificial neural network [23]. Facing a huge amount of data, it is necessary to choose the most appropriate data handling technology. Data cleaning is the first and most important step, avoiding the waste of analysis resources, or even the 'Garbage in, garbage out' phenomenon [24]. Perera et al. proposed a new digital model and built a data handling framework with pre-processing and post-processing units, based on the proposed digital model [25]. Raptodimos et al. proposed an integrated method based on an artificial neural network (ANN), which applies cross-clustering and self-organising mapping to cluster data, and then realises the main engine fault diagnosis [26]. Vanem et al. used unsupervised machine learning technology to analyse sensor data and monitor marine diesel engine anomalies [27]. Perera et al. introduced the expectation maximisation (EM) algorithm and Gaussian Mixture Models (GMMs) for the main engine speed-power clustering; analysis showed that data could be divided into three clustering centres [28]. Perera et al. studied the clustering methods again and obtained great relationships between ship performance and navigation information by principal component analysis (PCA) [29]. Yan et al. proposed the application of a distributed parallel K-means clustering algorithm for path division. Later, they used the Map Reduce-based k-average algorithm to analyse the environmental factors of different route segments [30, 31]. Adland et al. evaluated the effect of hull fouling on fuel consumption,

by regression analysis of daily fuel consumption and ship speed [32]. However, the influence of the decrease in diesel engine performance on the increase in fuel consumption was ignored.

In summary, most of the previous studies focused on the application of big data to consider the impact of environmental factors on ship energy efficiency and adopted intelligent algorithms, to assist ship fuel-saving decisions. However, the energy efficiency caused by the degradation of diesel engine performance and the impact of operating conditions on diesel engine performance is widely ignored and most of the black box models were adopted, so the analysis results were difficult to explain clearly. For energy efficiency monitoring and optimisation models, we need to balance the complexity of the model with the interpretability of the results. Based on this, models are usually classified as black box models or white box models. The black box model focuses on high precision of input and output. The white box model is characterised by physical characteristics, focusing on the interaction and logical relationship between various factors. The grey box model lies between the white box model and the black box model and has both advantages [33].

This study demonstrates a ship energy efficiency big data platform, based on the Beidou system, and some functional modules of the platform have also been described in previous work [18, 34]. This paper focuses on the functional modules, including data statistics, clustering, and engine performance analysis. A method of main engine performance evaluation is proposed, based on two years' of monitoring data from an operational ship. Using data statistics, machine learning, and physics-based methods, the comparison curves of diesel engine performance under different working conditions were obtained as the basis of the main engine performance evaluation.

Compared with previous studies, the contributions of this paper are:

- This study makes up for the fact that there are few applications of big data to evaluate the ship's main engine performance in previous studies.
- Previous studies have typically used only one of two approaches: unsupervised machine learning or physics-based analysis. This paper adopts the idea of the grey box model and combines the two methods to consider the accuracy and interpretability of the analysis results.
- The ship energy efficiency big data platform constructed in this study is universal and can also provide information support for energy-saving decisions of other diesel propulsion ships.

The rest of this paper is organised as follows: the description of the platform framework, techniques, and approaches is presented in Section II; data distribution statistics for the main engine operating situation are presented in Section III; the data cluster for the operational data is presented in Section IV; and the analysis results are presented in Section V. The conclusion is provided in Section VI.

DESCRIPTION OF PLATFORM FRAMEWORK, TECHNIQUES, AND APPROACHES

OVERALL FRAMEWORK OF BIG DATA PLATFORM

The framework of the big data platform is shown in Fig. 1. The on-board database records the main engine status, ship status, and ship loading status in real-time. In addition, it records the fuel consumption of the main engine from the high-precision mass flow meter. On the user interface of the on-board software, relevant monitoring data and curves are displayed, as well as the energy flow. Through the Beidou system, the data is transmitted to the onshore database in real time. Ship managers can carry out statistical analysis, clustering, polynomial curve fitting, and physics-based analysis with the collected data. The analysis results can be used as the basis for evaluating the energy efficiency of the ship and the performance of the main engine, which helps to make fuel-saving decisions and maintenance plans.

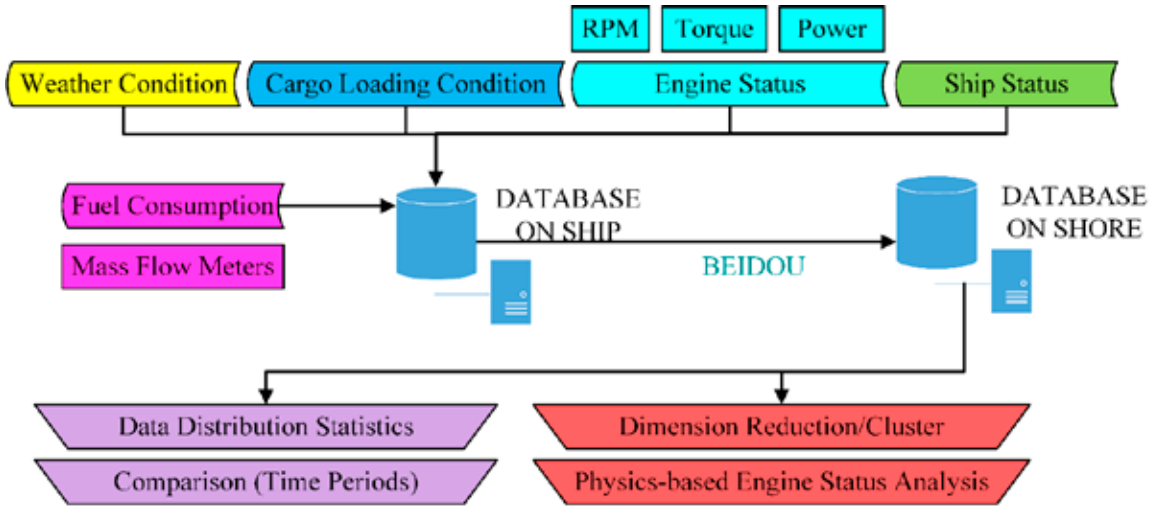

Fig. 1. Framework of big data platform

The on-board sensors measure the fuel consumption, main engine status, ship status, and ship loading status in real-time. Table 1 details some relevant data descriptions. The data comes from different systems and their acquisition frequency is not the same. The fuel consumption is read from the mass flow meter each second, using the RS485 communication device. The data on the engine status is sent out from the monitoring and alarm system every 30 seconds, via the Ethernet communication. Data such as ship speed and draft, relative wind speed and direction are read from the system on the bridge with the serial communication, and their frequency is about 10 seconds. To integrate all the systems with the same intervals, our platform records data every minute. Data from the sensors with a frequency greater than one minute are averaged, which also acts as a filter. In addition to the mean data, the standard deviation of high-frequency data is also calculated and recorded. The data is flagged as being abnormal if the standard deviation is higher than a certain threshold.

Tab. 1. Data Description

Categories	Items	Unit	Description
Fuel Consumption Rate	MEActFOCon	kg/h	fuel consumption rate
Main Engine Status	MERPM	r/min	main engine shaft speed
	METorque	kN*m	main engine shaft torque
	MEShaftPow	kW	main engine shaft power
Ship Status	ShipSpdToWater	knot	ship's water-referenced speed
	ShipSlip	%	slip ratio of propeller
Cargo Loading Status	ShipDraft	m	ship's draft

The MESFOC_kw is the specific fuel consumption of the main engine, see Eq. (1). Its unit is g/kWh. It shows how much fuel a diesel engine needs to produce 1 kW of power in one hour. This index can also reflect the economic performance of the engine and can be used for the analysis of engine performance degradation. Eq. (1) is affected by the lower calorific value (LCV) of the fuel. The ship studied in this work used marine diesel oil (MDO) and heavy fuel oil (HFO), which have different LCVs. However, when using HFO, marine engineers use the same type of fuel. For this concern, the platform automatically distinguishes two kinds of oil, with their different operating temperatures, to reduce the operations of engineers. Density is also recorded from the flow meter, for manual inspection. When the engine was running on HFO, this accounts for most of the available data. It is assumed that the used HFO has the same LCV in the current study, and the platform may also add a field to record the LCV for further consideration in future studies.

$$MESFOC\_kw = \frac{MEActFOCon}{MEShaftPow} * 1000 \quad (1)$$

The propeller's slip rate is an important factor that characterises the main engine load; it is called ShipSlip in the system. The ShipSlip is calculated by Eq. (2), which is determined by the water reference speed v_s and the shaft speed n_{ME}. In Eq. (2), H is the pitch of the propeller, which is the distance that the propeller advances when it rotates one revolution.

$$ShipSlip = (1 - v_s * \frac{1852}{n_{ME}} * H * 60) * 100 \quad (2)$$

Since the vast majority of vessels use diesel engines, the matter of their efficient and safe operation is an ongoing issue [36]. A big data platform was installed on a 2400 TEU container ship in October 2019 and the data obtained from January 1st to July 31st, 2020, as well as the same period in 2021. These are taken as an example to illustrate the effectiveness of the proposed method. The ship uses a two-stroke low-speed diesel engine (MAN B&W 7S60ME-C10.5, MCR: 13,700 kW * 97 r/min) as the main engine. The main engine directly drives the fixed pitch propeller. The propeller has four blades and an average pitch of 6.134 m. Three diesel generators, one exhaust gas boiler, and one oil-fired boiler are installed on the ship.

Based on these energy efficiency-related data, approaches such as numerical distribution statistics, machine learning, and physics-based analysis were used for engine performance analysis.

In the data pre-processing, the data were removed while the vessel was at berth. The system on the bridge sometimes does not send data because the system may be shut down. These data were also removed. In this work, the performance of the engine under stable operation was studied, so only the data of specific fuel consumption in the range of 160-260 g/(kW*h) was kept. Table 2 shows a sample of the values of the variables.

Tab. 2. A sample of the values

PCDate	PCTime	MEActFOCons	MESFOC_kw	MESFOC_nmile	ShipSpdToWater
2020/5/24	9:01:00	1496.718	190	83.76997	17.867
MERpm	METorque	MEShaftPow	WindSpd	WindDir	Latitude
86	875.833	7877.5	29.017	239	10.50 N
ShipSpd	ShipHeel	ShipTrim	ShipDraft	ShipSlip	Longitude
17.651	0.29	0.382	8.651	-2.79775	126.00 E

DESCRIPTION OF TECHNIQUES

The platform applied data statistics, clustering, and curve fitting to fulfil the study.

Numerical Distribution Statistics

Statistics aim to extrapolate the ships' overall running and operating situations, based on the data. The analysis and comparison of data distribution are helpful to understanding the difference in working conditions of different ships or the same ship at different times. In numerical distribution statistics, the probability mass function (PMF) is a normalised histogram that shows the frequency of occurrence of each value, typically for discrete variables. The good performance of PMF needs to deal with the grouping interval, while the cumulative distribution function (CDF) does not, and it can explain the difference between the distributions more clearly. PMF and CDF are both applied to the data distribution. As in Eq. (3) and Eq. (4), the PMF of the value x in the set X is the probability of x in X, while the CDF of the value x in the set X is the cumulative probability of the values in X that are less than x.

$$pmf_X(x) = \mathrm{P}(X = x) \tag{3}$$

$$cdf_X(x) = \mathrm{P}(X <= x) \tag{4}$$

Data Clustering

The basic idea of clustering is to construct k data clusters for a given data set with n samples. Generally, $k \leq n$; each cluster contains at least one sample and each sample only belongs to one cluster. Clustering methods divide data into k clusters, based on data distance or probability density models. In this paper, two different methods were used in the clustering process: the Gaussian mixture model (GMM) and density-based noise application spatial clustering (DBSCAN). The GMM is based on the assumption that the data conforms to the Gaussian statistical model and iteratively improves the parameters of the estimated model by using the Expectation-Maximisation (EM) algorithm. The algorithm can obtain the mean and covariance matrix of the clusters and get the weights of different clusters. When predicting the cluster category of a sample, the probability that the sample belongs to different clusters can be estimated. The GMM algorithm needs to input the number of clusters first, and then iteratively converges to the centre of the data cluster.

DBSCAN is a density-based clustering algorithm [35]. It can divide the region with a high-enough density into clusters and find cluster shapes in the noise data. DBSCAN describes the compactness of the sample set based on data density. Parameters (EPS, min_samples) are used to describe the compactness of the sample distribution in the neighbourhoods. Wherein, 'EPS' describes the small distance of neighbourhoods belonging to the same cluster, and 'min_samples' describes the minimum number of samples in the cluster.

If the number of samples included in the 'EPS' neighbourhood of sample x_i is not less than 'min_samples', i.e. $|N_{EPS}(x_i)| \geq \text{min\_samples}$, then x_i is called the core point. Otherwise, if $|N_{EPS}(x_i)| < \text{min\_samples}$, then x_i may be in the neighbourhood of other core points, which is called a boundary point. If x_i is neither a core point nor a boundary point, it is a noise point. The DBSCAN algorithm also defines the concepts of density direct, density reachable, and density connected. The basic process of the DBSCAN clustering algorithm is to determine all the core points according to the parameters (EPS, min_samples). It needs to find the sample with the highest density to generate a cluster and repeat the process to divide the data samples.

In this paper, we used Python-based Scikit-Learn to perform DBSCAN and GMM clustering algorithms on the pre-processed data, to find 'clusters' [37].

Polynomial curve fitting

Polynomial fitting is used to find the unknown parameters in the empirical formula dominated by a known law or model hypothesis through several known points. For example, given a function $f(\boldsymbol{x}; a_0, a_1, a_2, \ldots, a_m) = a_0 + a_1x_1 + a_2x_2 + \ldots + a_mx_m$. $\boldsymbol{x}$ represents an m-dimensional sample vector. $a_0, a_1, \ldots, a_m$ are the parameters to be determined. In general, given a set of samples $(\boldsymbol{x}_1, \boldsymbol{x}_2, \ldots, \boldsymbol{x}_n)$ whose measured function values are $(y_1, y_2, \ldots, y_n)$, it is possible to determine $(a_1, a_2, ..., a_m)$ by the least square method. A polynomial curve fit, as in Eq. (5) and (6), finds the parameter that minimises the squared value of the deviation between the output of the function and the measured value.

$$f(\boldsymbol{x}; a_0, a_1, \cdots, a_m) = a_0 + a_1x_1 + \cdots + a_mx_m \tag{5}$$

$$\arg\min_{a_0, a_1, \cdots, a_n} \sum_{i=1}^{n} [f(\boldsymbol{x}_i; a_0, a_1, \cdots, a_m) - y_i]^2 \tag{6}$$

The least square method is used to perform polynomial curve-fitting on the relationship between ME shaft speed - ME shaft power, ME shaft power – MESFOC_kw, and ME shaft speed - MESFOC_kw to further study the characteristics of the engine.

Physics-based Analysis

The effective power and specific fuel consumption of the main engine changes with the operating conditions of the diesel engine. The system carries out the performance evaluation of the main engine from three kinds of curves, which are the propulsion characteristics curve, the load characteristics curve, and the speed characteristics curve. The relationship between the main engine shaft power MEShaftPow and the main engine shaft speed MERPM during a ship's operation is cubic. This relationship is the propulsion characteristic of the main engine. The data of main engine shaft power, shaft speed, and specific fuel consumption rate MESFOC_kw are filtered in the cluster centres. The relationships between MEShaftPow - MESFOC_kw and MERPM - MESFOC_kw, which are the load and speed characteristics of the main engine, are obtained through data query and curve fitting by a self-developed software, written in C#.

DATA DISTRIBUTION STATISTICS FOR THE MAIN ENGINE OPERATING SITUATION

Using the method of distribution statistics, the two periods from January 1 to July 31 in 2020, and the same period in 2021, are taken as the comparison periods to compare the main engine status and the cargo loading status.

COMPARISON OF THE OPERATING STATUS OF THE MAIN ENGINE

Fig. 2 to Fig. 4 show the PMF and CDF of main engine shaft speed MERPM, main engine shaft power MEShaftPow and ship water reference speed ShipSpdToWater during the observation period. It can be seen that the MERPM is often set at 47, 62, 77, 80, and 85 r/min on board and the MEShaftPow is also concentrated in the corresponding section. While the ship is sailing at sea, most of the load of the main engine comes from overcoming the navigation resistance under still water and part of the power is affected by wind, current, wave, and cargo loading, etc. The ship usually needs to attain a certain speed to transfer goods in time. However, at the same ship speed, the ship resistance also changes with the weather and loading conditions. Therefore, the shaft power of the main engine fluctuates with the shipload. As shown in Fig. 4, the ship water reference speed ShipSpdToWater has three obvious operation centres: 9.0, 12.5, and 16.0 knots.

It can also be seen from Fig. 2 to Fig.4 that the recorded main engine shaft speed MERPM and main engine shaft power MEShaftPow are more often in the high load range in 2021, than in the same period in 2020, so the ship's speed also increases. This is due to the increased volume of containers in 2021 and the need for vessels to speed up their cargo turnover.

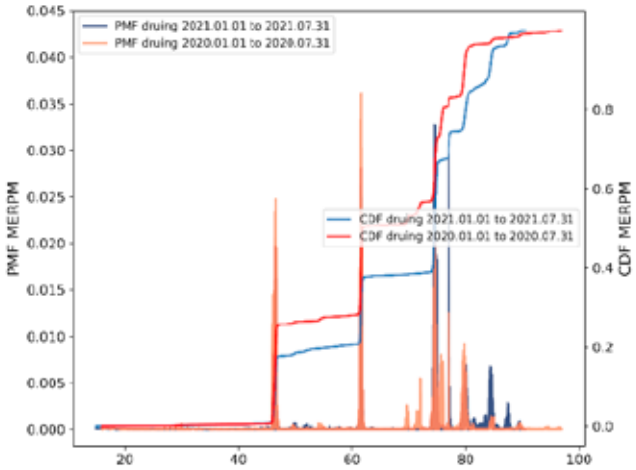

Fig. 2. PMF and CDF of main engine shaft speed (comparison between 2020 and 2021)

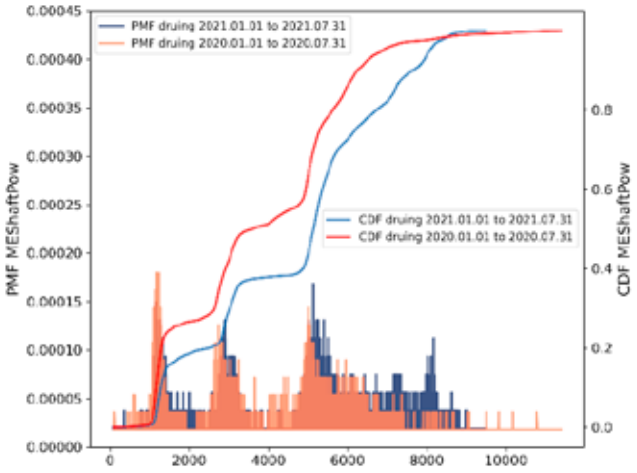

Fig. 3. PMF and CDF of main engine shaft power (comparison between 2020 and 2021)

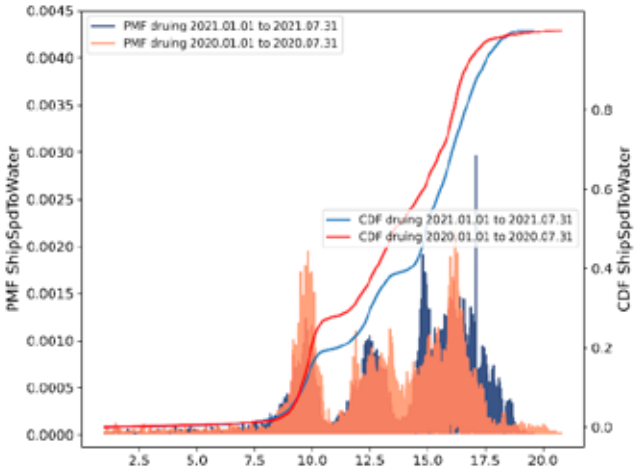

Fig. 4. PMF and CDF of water referenced ship speed (comparison between 2020 and 2021)

However, as shown in Fig. 5, the specific fuel consumption of the main engine MESFOC_kw in 2021 is more inclined to the left than that in the same period in 2020. That is to say, the specific fuel consumption is relatively low in 2021 because the main engine runs more in the high-power area in 2021 than that in 2020. It is hard to identify the engine performance degradation by the data statistics, which needs to be further studied from the engine load characteristics.

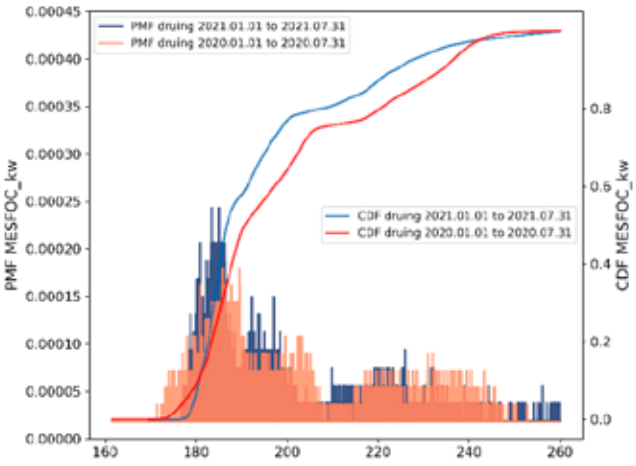

Fig. 5. PMF and CDF of main engine specific fuel consumption (comparison between 2020 and 2021)

COMPARISON OF SHIP BALLAST STATUS AND SHIP LOADING STATUS

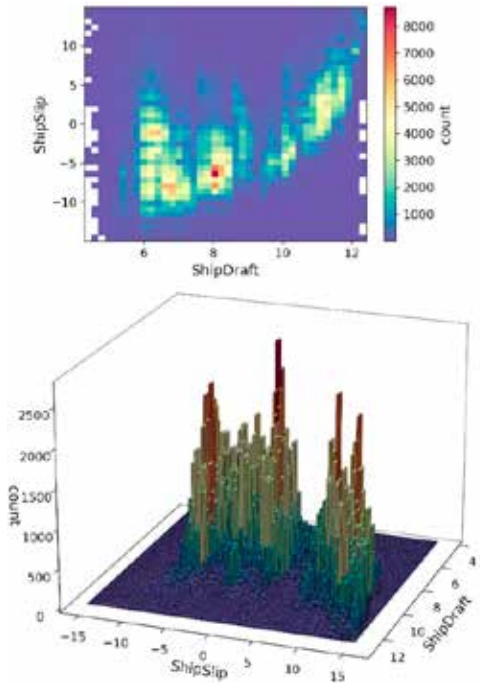

Fig. 6. Ship draft and propeller slip ratio (January 1st-July 31st, 2020)

Fig. 6 and Fig. 7 show the ship's draft ShipDraft and propeller slip ratio ShipSlip from January 1 to July 31 2020, and 2021, respectively. They show that the region of the ship's draft with the most data in 2020 is 8 m, while the region with the most data in 2021 is 11 m. The ship's draft significantly increases because the cargo volume of the ship in 2021 is significantly higher than that in the same period in 2020. In addition, both Fig.6 and Fig.7 show that, with the increase of the ship's draft, the propeller slip ratio increases as well, due to the increase of the ship's resistance.

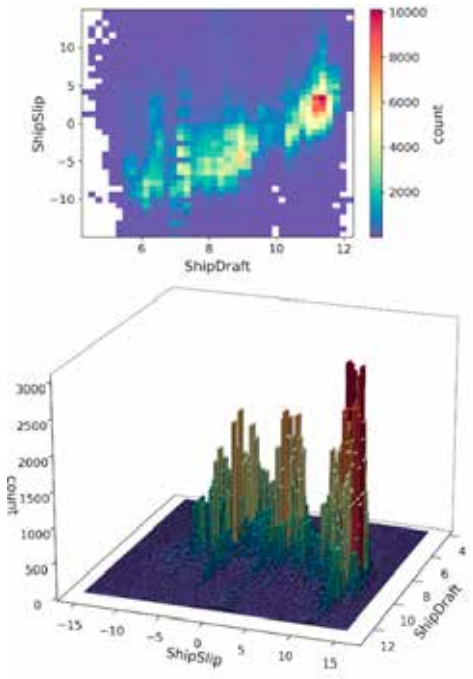

Fig. 7. Ship draft and propeller slip ratio (January 1st-July 31st, 2021)

The data in June 2020 is screened to show the ship draft effect on the main engine's load. In a month, the affect of the fouling of the ship's hull on the result is low. In the same period, the weather condition is similar. In addition, the relative wind speed is limited to the range 12-18 knots. The relationship between the main engine speed and the shaft power of the ship under ballast and full load conditions was studied. The data when the main engine runs in a stable manner is obtained. Under the ballast condition, the data of the ship's draft range is 6-7 m, and the data of the ship's draft range is 10.5-11.5 m under the full load condition. If two or more of the same data are at nearly the same engine speed, they are averaged at intervals of 0.2 *r/min* of engine speed. Fig. 8 shows the results. When the ship is in a ballast state, the data points of the main engine shaft speed and power are displayed as purple triangles; when the ship is fully loaded, they are displayed as yellow circles. On the same horizontal axis, the yellow circles are slightly higher than the purple triangles onźthe vertical axis. Loading cargo will increase the propeller slip ratio, leading to an increase in the load of the main engine. The average shaft speed of the ship at full load is 65.71 r/min and the required average shaft power is 4529.73 kW. The average shaft speed of the ship in ballast is 67.30 r/min and the required average shaft power is 4247.38 kW. Cargo loading causes the average shaft speed to decrease by 1.59 r/min, while the average power increases by 282.34 kW.

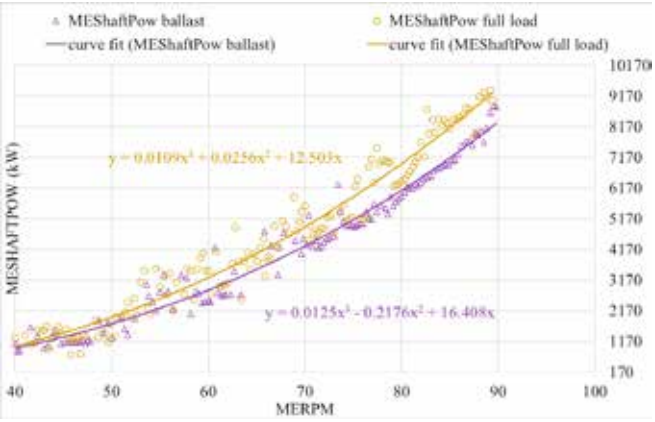

Fig.8 . Propulsion characteristics curves of the main engine (comparison under the ship in ballast and full load conditions)

CLUSTER OF OPERATION DATA

The pre-processed data distribution can be displayed as variable histograms. Fig. 9, Fig. 10, and Fig. 11 show the histograms of energy efficiency-related variables of the main engine with all data, ballast state data, and full load state data, respectively. In the figures, the horizontal axis is the variables' area and the vertical axis is the variables' count. The histogram results show that all variables are within a reasonable range. Moreover, the main engine mainly operates in the three power centres.

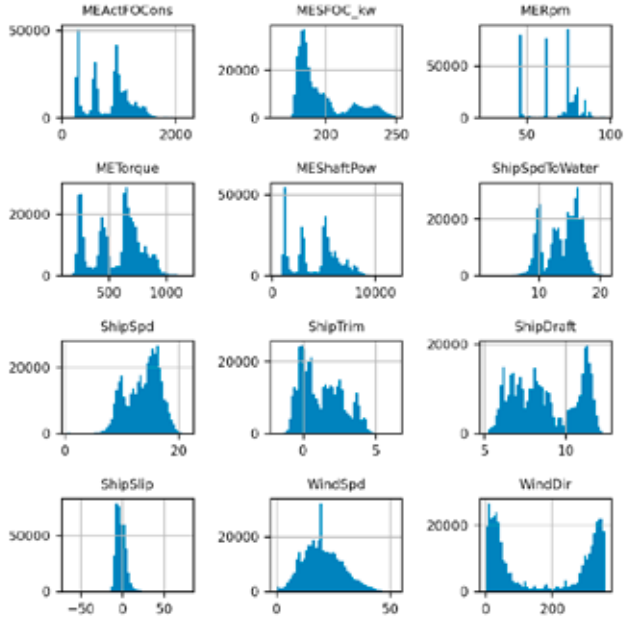

Fig. 9. Histogram of variables after data pre-processing (all data)

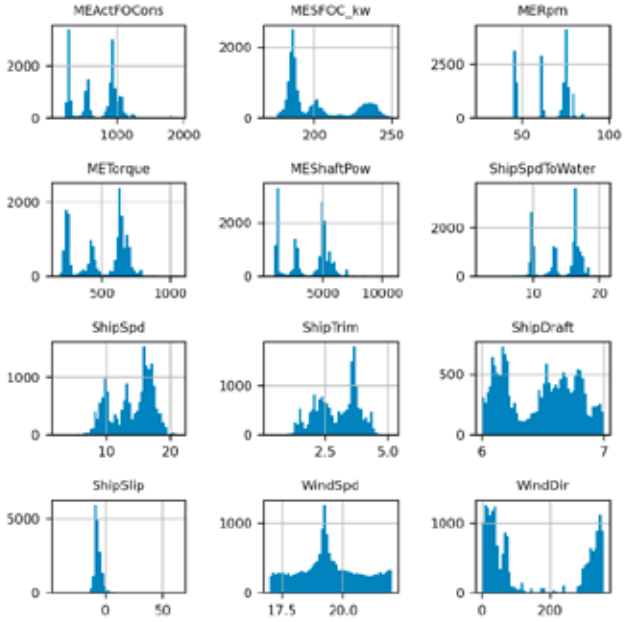

Fig. 10. Histogram of variables after data pre-processing under ballast state (relative wind speed in 12-18 knots and ship draft in 6-7 m)

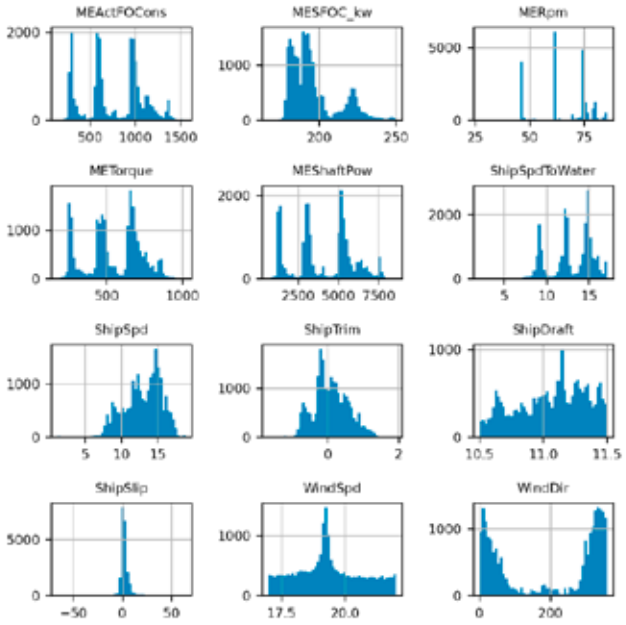

Fig. 11. Histogram of variables after data pre-processing under full load state (relative wind speed in 12-18 knots and ship draft in 10.5-11.5 m)

To explore the correlation between variables, we conducted Pearson correlation tests on them. Fig. 12 shows the Pearson correlation between all variables. It can be seen that the fuel consumption rate of the main engine is not only closely related to the state of the main engine but also has a certain correlation with the ship's draft, trim, and relative wind speed. Although this correlation is small, it should also be considered in the study. The ship's trim is highly related to the ship's draft. To further consider factors such as ship loading status

and weather conditions, the study further selects the same relative wind speed range to cluster similar weather. Data are also constrained under full load and ballast conditions, to remove the effects of vessel loading variations.

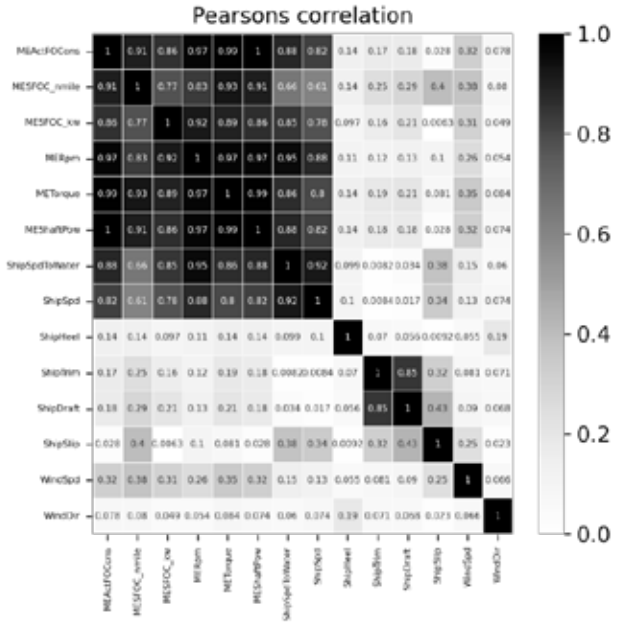

Fig. 12 Pearson correlation of the data (all data)

In this study, GMM and DBSCAN were combined for data clustering analysis. The general idea is to set the neighbourhood size (EPS) of DBSCAN to 3 and the minimum number of samples in the neighbourhood (min_samples) to 6, in order to obtain the frequent operation area of the main engine. Then GMM is applied to the cluster analysis of five variables (engine shaft speed MERPM, engine shaft power MEShaftPow, engine fuel consumption rate MEActFOCon, the specific fuel consumption of the main engine MESFOC, and water reference speed ShipSpdToWater) and three cluster centres are obtained. To consider the effects of the ship's loading status, weather conditions, and other factors, on the performance of the main engine, the cluster analysis was carried out on all data, ballast state data, and full load data, respectively.

Cluster analysis of all data

The cluster analysis results of all data are shown in Table 3 and Fig. 13-16. The three dark blue data clusters in Fig. 13 show the areas where the main engine often runs. Table 3 shows the three clustering centres and the clustering results are very consistent with the statistical analysis of data distribution. For a more intuitive display, Fig. 14 is a visualisation of three-dimensional data clusters of shaft speed, power, and fuel consumption rate, Fig. 15 displays two-dimensional data clusters of shaft speed and shaft power, and Fig. 16 is a visualisation of two-dimensional data clusters of water reference speed and shaft power.

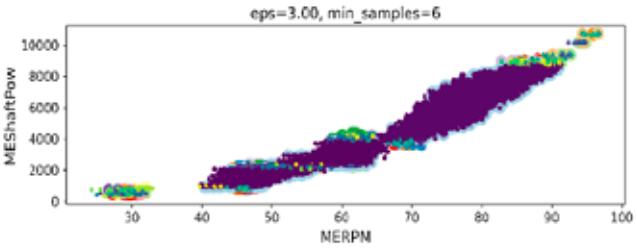

Fig. 13. Clustering analysis of shaft speed and power by DBSCAN in all states

Tab. 3. Clustering centre (All data)

Cluster centre	MERPM (r/min)	MEShaftPow (kW)	MEActFOCon (kg/h)	MESFOC (g/kw*h)	ShipSpdToWater (knot)
Cluster centre 1	46.56	1294.62	293.04	227.80	9.53
Cluster centre 2	78.10	6096.09	1123.29	184.68	16.07
Cluster centre 3	61.48	2970.05	591.04	199.43	12.60

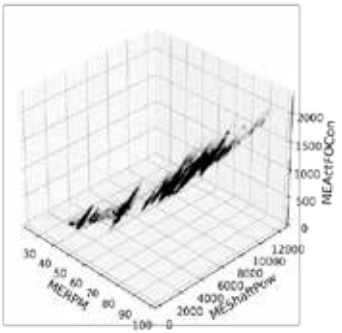

Fig. 14. Clustering analysis of shaft speed, power and fuel consumption rate by GMM in all states

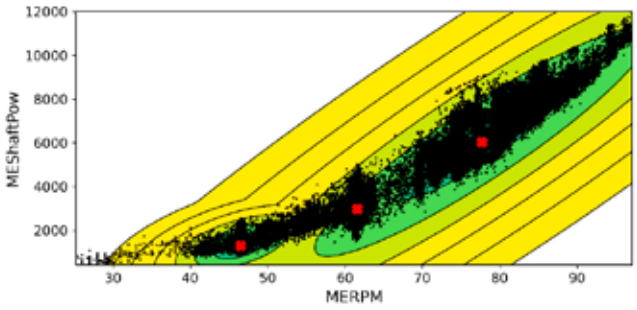

Fig. 15. Clustering analysis of shaft speed and power by GMM of all data

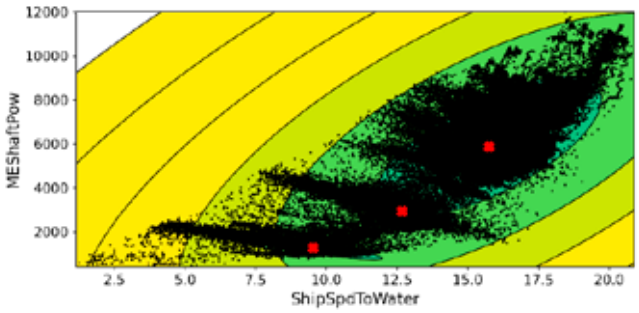

Fig. 16. Clustering analysis of water referenced ship speed and shaft power by GMM of all data

Clustering analysis of data under ballast and full load conditions

With the same steps (DBSCAN is used to determine three clusters and GMM is used to determine the cluster centres of key variables) and settings (EPS = 3, min_samples = 6), cluster analysis was performed on the data of ships with ballast and full load state, respectively. The cluster centres obtained from the analysis are shown in Tables 4 and 5.

Tab. 4. Clustering centre (data under relative wind speed in 12-18 knots and ballast state)

Cluster centre	MERPM (r/min)	MEShaftPow (kW)	MEActFOCon (kg/h)	MESFOC (g/kw*h)	ShipSpdToWater (knot)
Cluster centre 1	46.42	1194.62	293.04	234.04	9.84
Cluster centre 2	76.83	5469.11	1013.31	185.63	16.80
Cluster centre 3	60.46	2708.24	548.33	203.84	12.73

Tab. 5. Clustering centre (data under relative wind speed in 12-18 knots and full load state)

Cluster centre	MERPM (r/min)	MEShaftPow (kW)	MEActFOCon (kg/h)	MESFOC (g/kw*h)	ShipSpdToWater (knot)
Cluster centre 1	46.86	1433.69	314.81	221.08	9.10
Cluster centre 2	76.37	5779.90	1072.69	186.00	15.06
Cluster centre 3	61.57	3085.68	604.20	196.02	12.14

These cluster centres are areas with large amounts of data. They can be used to set the fuel consumption rate and the shaft speed in the mechanism analysis of the speed characteristic curve and the load characteristic curve.

MECHANISM ANALYSIS RESULTS

In the three clustering centres, we applied the polynomial curve fitting to fit the relationship between the key indicators of the main engine. Firstly, we took the three cluster centres of shaft speed MERPM generated by GMM as the set value for the data query and fitted the curve to obtain the relationship between MEShaftPow - MESFOC_kw of the main engine, which is the load characteristic curve. Then we took the fuel consumption rate MEActFOCon of cluster centre 2 as the set value for the data query, and fitted the curve to obtain the relationship between MERPM - MESFOC_kw, i.e. the speed characteristic curve. These characteristic curves help us to understand the changing trends of the main engine performance.

COMPARISON OF MAIN ENGINE LOAD CHARACTERISTIC CURVES IN TWO PERIODS

Fig. 17 and 18 are the correlation diagrams of MEShaftPow - MESFOC_kw at the cluster centres under ballast and full load states, respectively. Fig. 17 and 18 both show that the main engine's specific fuel consumption MESFOC_kw in 2021 was higher than that in 2020. Tables 6 and 7 list the average main engine shaft power (average MEShaftPow) and the average specific fuel consumption (average MESFOC_kw) of the load characteristic curves in 2020 and 2021. In summary, the data of both ballast and full load conditions show that the specific fuel consumption rate of the engine has increased due to engine degradation. The parent engine test data in the manual shows that the specific fuel consumption rate at 50% MCR is 167.8 g/kWh, and the testing fuel LCV is 42009.20 kJ/kg. The measured data of the engine in actual operation is higher than the engine test. The measured data is reasonable since the actual operating conditions are more severe.

Tab. 5. Average MEShaftPow and MESFOC_kw (load characteristic curves under ballast state)

Cluster centre	2020		2021	
	MEShaftPow	MESFOC_kw	MEShaftPow	MESFOC_kw
Cluster centre 1	11.66% MCR	222.28 g/kWh	11.01% MCR	224.01 g/kWh
Cluster centre 2	39.93% MCR	185.90 g/kWh	39.84% MCR	186.73 g/kWh
Cluster centre 3	22.00% MCR	199.66 g/kWh	22.04% MCR	205.08 g/kWh

Tab. 6. Average MEShaftPow and MESFOC_kw (load characteristic curves under full load state)

Cluster centre	2020		2021	
	MEShaftPow	MESFOC_kw	MEShaftPow	MESFOC_kw
Cluster centre 1	14.07% MCR	213.43 g/kWh	13.98% MCR	215.80 g/kWh
Cluster centre 2	47.66% MCR	183.78 g/kWh	47.27% MCR	185.94 g/kWh
Cluster centre 3	25.03% MCR	194.26 g/kWh	25.00% MCR	195.37 g/kWh

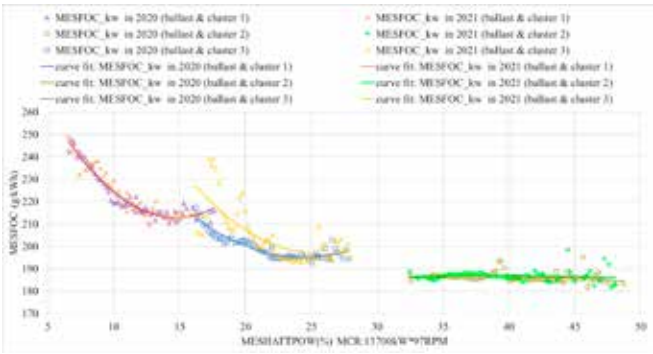

Fig. 17. Load characteristic curve of main engine shaft power - specific fuel consumption at cluster centres of ballast state

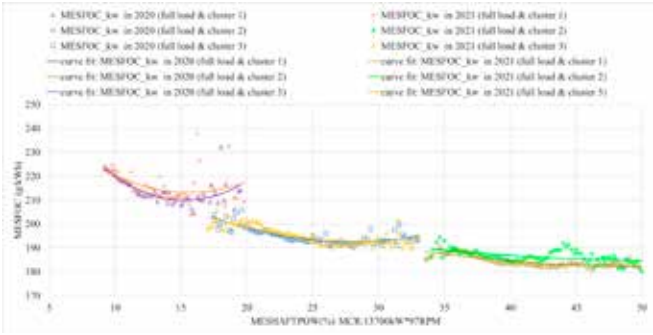

Fig. 18. Load characteristic curve of main engine shaft power - specific fuel consumption at cluster centres of full load state

COMPARISON OF MAIN ENGINE SPEED CHARACTERISTIC CURVES IN TWO PERIODS

The speed characteristic curves of the ship in the ballast and full load states, during the comparison periods, are created at cluster centre 2, as shown in Fig. 19.

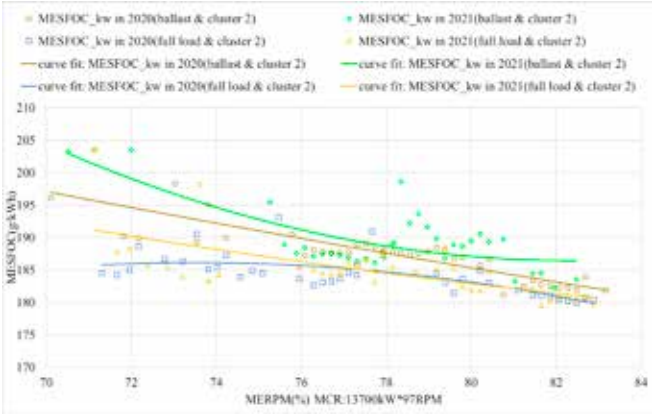

Fig.19. Speed characteristic curve of main engine shaft speed - specific fuel consumption at cluster centre 2 of ballast & full load states

The MEActFOCon of cluster centre 2 in the full load state is 1072.69 kg/h, while that in the ballast state is 1013.31 kg/h. At the query point, the engine load in the full load state is a little higher than in the ballast state, and so MESFOC_kw of the speed characteristic curve in the full load state is a little lower than that in the ballast state. Although the results also show that the specific fuel consumption rate in 2021 was higher than in 2020, the amount of data in the speed characteristic curve is still relatively small, and it is necessary to collect more data for further research.

CONCLUSION

This paper presents a main engine performance monitoring method based on energy efficiency big data. The method combines distribution statistics, clustering, and polynomial curve fitting to obtain the propulsion characteristics and load characteristic curves, as the basis of performance degradation monitoring and maintenance schedule of the main engine. The test results show that this method can effectively monitor the degradation of engine performance.

This research can be used as an important basis for creating a maintenance schedule for main marine engines. In the future, the ship maintenance schedule can be determined automatically, by developing the ship's intelligent energy efficiency system, which should consist of various autonomous technologies, such as machine learning (ML) and artificial intelligence (AI) technologies, assisting in intelligent monitoring, forecasting, and making auxiliary fuel-saving decisions.

ACKNOWLEDGMENT

This work was supported in part by the National Natural Science Foundation of China (52001195, 61873161) and the Science & Technology Commission of Shanghai Municipality and Shanghai Engineering Research Center of Ship Intelligent Maintenance and Energy Efficiency (20DZ2252300).

REFERENCES

1. B. Qiao, W. He, Y. Tian, Y. Liu, O. Cai, and Y. Li, "Ship emission reduction effect evaluation of air pollution control countermeasures," *Transportation Research Procedia*, vol. 25, pp. 3606-3618, 2017, doi: 10.1016/j.trpro.2017.05.325.

2. F. Jasper, H. Shinichi et al., "Fourth IMO Greenhouse Gas Study 2020," *International Maritime Organisation (IMO)*, London, UK, 2020.

3. V. Kuznetsov, B. Dymo, S. Kuznetsova, M. Bondarenko, and A. Voloshyn, "Improvement of the cargo fleet vessels power plants ecological indexes by development of the exhaust gas systems," *Polish Maritime Research,* vol. 28, pp. 97-104, 2021, doi: 10.2478/pomr-2021-0009.

4. I. Ančić and A. Šestan, "Influence of the required EEDI reduction factor on the CO_2 emission from bulk carriers,"

Energy Policy, vol. 84, pp. 107-116, 2015, doi: 10.1016/j.enpol.2015.04.031.

5. E.K. Hansen, H.B. Rasmussen, and M. Lützen, "Making shipping more carbon-friendly? Exploring ship energy efficiency management plans in legislation and practice," *Energy Research & Social Science*, vol. 65, pp. 101459, 2020, doi: 10.1016/j.erss.2020.101459.

6. M. Kalajdžić, M. Vasilev, and N. Momčilović, "Power Reduction Considerations for Bulk Carriers with respect to Novel Energy Efficiency Regulations," *Brodogradnja: Teorija i praksa brodogradnje i pomorske tehnike*, vol. 73, pp. 79-92, 2022, doi: 10.21278/brod72205.

7. L. Fedi, "The Monitoring, Reporting and Verification of Ships' Carbon Dioxide Emissions: A European Substantial Policy Measure towards Accurate and Transparent Carbon Dioxide Quantification," *Ocean Yearbook Online*, vol. 31, pp. 381-417, 2017, doi: 10.1163/22116001-03101015.

8. W. Tarełko, "The effect of hull biofouling on parameters characterising ship propulsion system efficiency," Polish Maritime Research, vol. 21, pp. 27-34, 2014, doi: 10.2478/pomr-2014-0038.

9. P. Król, «Hydrodynamic state of art review: rotor–stator marine propulsor systems design,» *Polish Maritime Research,* vol. 28, pp. 72-82, 2021, doi: 10.2478/pomr-2021-0007.

10. P. Puzdrowska, «Diagnostic information analysis of quickly changing temperature of exhaust gas from marine diesel engine. Part i single factor analysis,» *Polish Maritime Research,* vol. 28, pp. 97-106, 2021, doi: 10.2478/pomr-2021-0052.

11. P. Król, "Blade section profile array lifting surface design method for marine screw propeller blade," *Polish Maritime Research,* vol. 26, pp. 134-141, 2019, doi: 10.2478/pomr-2019-0075.

12. K. Rudzki and W. Tarelko, "A decision-making system supporting selection of commanded outputs for a ship's propulsion system with a controllable pitch propeller," *Ocean Engineering,* vol. 126, pp. 254-264, 2016, doi: 10.1016/j.oceaneng.2016.09.018

13. R. Varbanets, V. Zalozh, A. Shakhov, I. Savelieva, and V. Piterska, "Determination of top dead centre location based on the marine diesel engine indicator diagram analysis," *Diagnostyka,* vol. 21, pp. 51-60, 2020, doi: 10.29354/diag/116585.

14. S. Park, S. W. Park, S. H. Rhee, S. B. Lee, J. E. Choi, and S. H.Kang, "Investigation on the wall function implementation for the prediction of ship resistance," *International Journal of Naval Architecture and Ocean Engineering*, vol. 5, pp. 33-46, 2013, doi: 10.2478/IJNAOE-2013-0116.

15. M.B. Samsul, "Blade cup method for cavitation reduction in marine propellers," *Polish Maritime Research*, 2021, doi: 10.2478/pomr-2021-0021, doi: 10.2478/pomr-2021-0021.

16. M.H. Ghaemi, "Performance and emission modelling and simulation of marine diesel engines using publicly available engine data," *Polish Maritime Research,* vol. 28, pp. 63-87, 2021, doi: 10.2478/pomr-2021-0050.

17. B.D. Brouer, C.V. Karsten, and D. Pisinger, "Big data optimisation in maritime logistics," *Big data optimisation: Recent developments and challenges. Springer, Cham*, vol. 18, pp. 319-344, 2016, doi: 10.1007/978-3-319-30265-2_14.

18. X. Zeng and M. Chen, "A Novel Big Data Collection System for Ship Energy Efficiency Monitoring and Analysis Based on BeiDou System," *Journal of Advanced Transportation*, vol. 2021, pp.1-10, 2021, doi: 10.1155/2021/9914720.

19. I. Zaman, K. Pazouki, R. Norman, S. Younessi, and S.Coleman, "Challenges and opportunities of big data analytics for upcoming regulations and future transformation of the shipping industry," *Procedia engineering*, vol. 194, pp. 537-544, 2017, doi: 10.1016/j.proeng.2017.08.182.

20. A. Fan, X. Yan, and Q. Yin, "A multisource information system for monitoring and improving ship energy efficiency," *Journal of Coastal Research,* vol.32, pp. 1235-1245, 2016, doi: 10.2112/JCOASTRES-D-15-00234.1.

21. J. Deng, J. Zeng, S. Mai, B. Jin, B. Yuan, Y. You. S. Lu, and M.Yang, «Analysis and prediction of ship energy efficiency using 6G big data internet of things and artificial intelligence technology,» *International Journal of System Assurance Engineering and Management,* vol. 12, pp. 824–834, 2021, doi: 10.1007/s13198-021-01116-9.

22. T. Niksa-Rynkiewicz, N. Szewczuk-Krypa, A. Witkowska, K. Cpałka, M. Zalasiński, and A. Cader, "Monitoring regenerative heat exchanger in steam power plant by making use of the recurrent neural network," *Journal of Artificial Intelligence and Soft Computing Research,* vol. 11, pp. 143-155, 2021, doi: 10.2478/jaiscr-2021-0009.

23. A. Witkowska and T. Niksa-Rynkiewicz, «Dynamically positioned ship steering making use of backstepping method and artificial neural networks,» *Polish Maritime Research,* vol. 25, pp. 5-12, 2018, doi: 10.2478/pomr-2018-0126.

24. S. García, J. Luengo, and F. Herrera, "Data preprocessing in data mining," *Cham, Switzerland: Springer International Publishing,* vol. 72, pp. 59-139, 2015, doi: 10.1007/978-3-319-10247-4.

25. L.P. Perera and B. Mo, "Ship performance and navigation information under high-dimensional digital models," *Journal of Marine Science and Technology,* vol. 25(1), pp. 59-139, 2020, doi: 10.1007/978-3-319-10247-4.

26. Y. Raptodimos and I. Lazakis, "Using artificial neural network-self-organising map for data clustering of marine engine condition monitoring applications," *Ships and Offshore Structures,* vol. 13, pp. 649-656, 2018, doi: 10.1080/17445302.2018.1443694.

27. E. Vanem and A. Brandsæter, "Unsupervised anomaly detection based on clustering methods and sensor data on a marine diesel engine," *Journal of Marine Engineering & Technology,* vol. 20, pp. 217-234, 2021, doi: 10.1080/20464177.2019.1633223.

28. L. P. Perera, and B. Mo, "Data analytics for capturing marine engine operating regions for ship performance monitoring," *International Conference on Offshore Mechanics and Arctic Engineering,* American Society of Mechanical Engineers, 2016, Vol. 49989, doi: 10.1115/OMAE2016-54168

29. L. P. Perera, and B. Mo, "Marine engine operating regions under principal component analysis to evaluate ship performance and navigation behaviour," IFAC-PapersOnLine, vol. 49(23), pp. 512-517, 2016, doi: 10.1016/j.ifacol.2016.10.487.

30. X. Yan, K. Wang, Y. Yuan, X. Jiang, and R. R. Negenborn, "Energy-efficient shipping: An application of big data analysis for optimizing engine speed of inland ships considering multiple environmental factors," Ocean Engineering, vol. 169, pp. 457-468, 2018, doi: 10.1016/j.oceaneng.2018.08.050.

31. K. Wang, X. Yan, Y. Yuan, X. Jiang, G. Lodewijks, and R. R. Negenborn, «Study on route division for ship energy efficiency optimisation based on big environment data,» *2017 4th International Conference on Transportation Information and Safety (ICTIS), IEEE,* pp. 111-116, 2017, doi: 10.1109/ICTIS.2017.8047752.

32. R. Adland, P. Cariou, H. Jia, and F. C. Wolff, "The energy efficiency effects of periodic ship hull cleaning," *Journal of Cleaner Production*, vol. 178, pp. 1–13, 2018, doi: 10.1016/j.jclepro.2017.12.247.

33. O. Loyola-Gonzalez, "Black box vs. white-box: Understanding their advantages and weaknesses from a practical point of view, " *IEEE Access,* vol. 7, pp. 154096–154113, 2019, doi: 10.1109/ACCESS.2019.2949286.

34. X. Zeng, M. Chen, H. Li and X. Wu, "A Data-Driven Intelligent Energy Efficiency Management System for Ships," *IEEE Intelligent Transportation Systems Magazine*, doi: 10.1109/MITS.2022.3153491.

35. M. Ester, H. P. Kriegel, J. Sander, and X. Xu, "A density-based algorithm for discovering clusters in large spatial databases with noise," *kdd,* vol. 96, pp. 226-231, 1996.

36. R. Varbanets, V. Klymenko, O. Fomin, V. Píštěk, P. Kučera, D. Minchev, A. Khrulev, and V. Zalozh, "Acoustic method for estimation of marine low-speed engine turbocharger parameters," Journal of Marine Science and Engineering, vol. 9, 2021, doi: 10.3390/jmse9030321.

37. A. GéRon, "Hands-on Machine Learning with Scikit-Learn and TensorFlow: Concepts, Tools, and Techniques to Build Intelligent Systems". *Sebastopol, CA, USA: O'Reilly Media,* 2017.

CONTACT WITH THE AUTHORS

Meng Liang
e-mail: liangmeng02@163.com

Shanghai Dianji University, Business School,
Shanghai
China

Mingzhi Chen

Shanghai Maritime University,
Merchant Marine College and Shanghai Engineering Research Center of Ship Intelligent Maintenance and Energy Efficiency, Shanghai
China